STOCKHOLM UNIVERSITY

DEPARTMENT OF PHYSICS

READ-OUT AND CALIBRATION OF A TILE CALORIMETER FOR ATLAS

S. TARDELL

USIP Report 97 - 07

June 1997
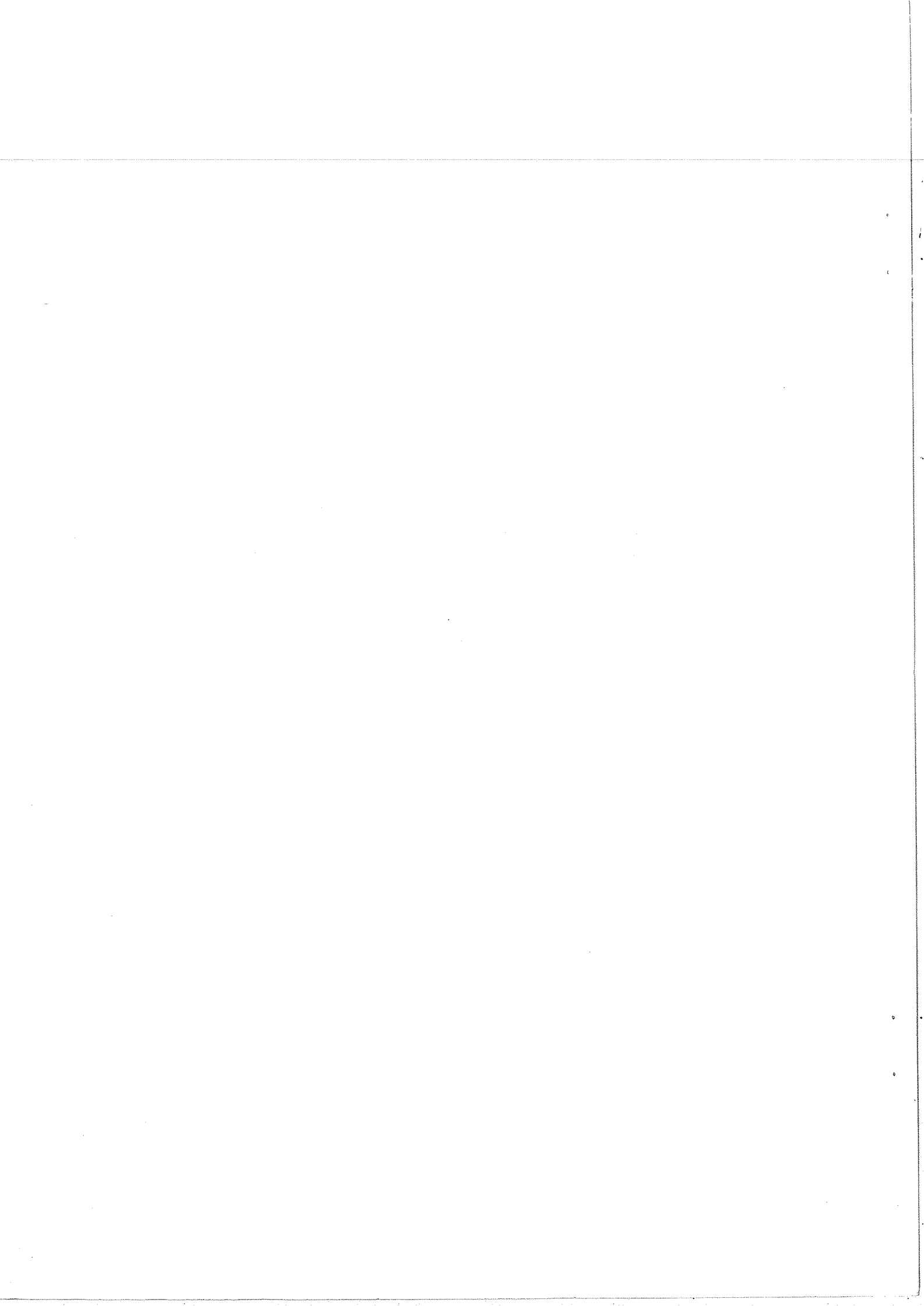
Thesis-1997-Tardell

Abstract

The read-out and calibration of a scintillating tiles hadronic calorimeter for ATLAS is discussed. Tests with prototypes of FERMI, a system of read-out electronics based on a dynamic range compressor reducing the dynamic range from 16 to 10 bits and a 40 MHz 10 bits sampling ADC, are presented. In comparison with a standard charge integrating read-out improvements in the resolution of 1% in the constant term are obtained.

Contents

1. Introduction

The last two decades have witnessed unprecedented triumphs for both the theoretical and experimental aspects of elementary particle physics leading up to a complete theory of matter and radiation up to energies of about 1 TeV. The Standard Model, the marriage of the theories of electroweak and strong interactions, accurately describes matter up to that energy, and there is no direct evidence that it does not prevail further. For theoretical reasons, we believe it does not. Theory hints us that the Standard Model is but a low energy limit of a larger theory, and that this new physics could, or even should, be in reach of the next generation experiments now in construction. The only unconfirmed part of the Standard Model is the mechanism for generating mass, through the Higgs boson. Even if this is discovered, the new physics beyond the Standard Model has to explain why the Higgs mechanism works the way it does.

At CERN, the Large Electron Positron collider, LEP, has successfully mapped out most of the Standard Model and determined its parameters with the utmost precision. In its first phase LEP was operating at or near the Z^0 pole; in its second phase, recently begun, LEP is entering a more exploratory phase and will search out energies up to slightly less than 200 GeV in centre-of-mass. What ultimately limits a machine of this type is the amount of energy lost per turn due to synchrotron radiation losses. It is likely that LEP is the largest of this kind of accelerator we will see.

To overcome this limitation the High Energy Physics community has turned to proton-proton colliders. The proton, being much heavier, can be accelerated to multi-TeV energies without unacceptable losses. The limiting factor here is instead the obtainable field in the bending magnets. The Large Hadron Collider, LHC, is just such a machine now being projected at CERN. LHC will be built inside the tunnel already housing LEP; the radius thus fixed, the energy is determined by the bending magnetic field of 8.4 tesla and the configuration of the magnets, to 7 TeV per beam or 14 TeV in centre-of-mass.

Since most of the physical questions to be put to this machine involve interactions with very low cross-sections, not only high energy, but also high luminosity is required. LHC is designed to provide luminosities in excess of $10^{34} \mathrm{cm}^{-2} \mathrm{s}^{-1}$. To achieve this, an inter-bunch spacing of 25 ns has been chosen. At these extremely high luminosities, about 10^9 collisions per second is expected. To operate success-

fully under these conditions is a very exacting requirement for an experiment.

ATLAS is one of the two general purpose experiments designed to operate at LHC and exploit its full discovery potential. ATLAS is characterized by a large muon spectrometer based on a large toroidal supraconducting magnet, efficient tracking, electron and photon identification and a very good electromagnetic calorimeter supplemented by good jet and missing transverse energy measurements giving fundamental handles to many interesting physics signals. The main hadron calorimeter is of an iron-scintillating tiles type, named "Tilecal".

The high rates put very special demands on the read-out electronics of the detector, to be able to pick up signals out of a constant background of stray QCD interactions spraying the detector, and also to be able to digitize both the faint muon signals and the largest signals expected with an acceptable resolution. An integrated solution, based on a compressor, a 40 MHz sampling ADC and a digital pipeline is activily being pursued for Tilecal.

Tilecal has been prototyped and tested in beam at the CERN SPS 1993–96. In the test beams 1995 and 96 the prototypes were partially equipped with this novel read-out electronics. A good calibration system is necessary for the detector in order to make optimal use of the intrinsic resolution of the calorimeter.

This thesis is organized as follows: Chapter 2 discusses the physics potential for LHC, and what some of the questions most yearning to get an answer are. Chapter 3 describes LHC and ATLAS. Chapter 4 goes through some preliminaries of hadron calorimetry. Chapter 5 describes the Tile calorimeter. Chapter 6 discusses the first large scale tests of Fermi, equipping part of the Tile calorimeter prototype in the 1995 beam tests. These tests are also the subject of the paper appended. This paper is to be submitted for publication in *Nucl. Instr. Meth.*.

2. Physics at the Large Hadron Collider

The Standard Model[1, 2, 3] describes Nature in terms of twelve matter particles and two types of interactions, the electroweak, mediated by the photon, $W^{\pm}$ and Z^0, and the strong, mediated by the gluons. No experiment so far has found any deviations from this description; instead the predictive power of the Standard Model has been very strong, the discovery of neutral currents and, subsequently, of the physical W and Z-bosons being prime examples (e.g. see [4]).

The precision electroweak measurements performed at LEP[5, 6, 7] can be used to check the validity of the Standard Model and to infer valuable information about its basic parameters. Also, the accuracy of these measurements make them sensitive to the top quark mass, m_t, and to the mass of the Higgs boson, m_H, through radiative corrections.

Except for the Higgs boson, which the theory requires to give mass to the fundamental particles, this model has been completely confirmed. Theoretical arguments do however exist indicating that the Standard Model is a low energy limit of a more fundamental theory. Such a theory is expected to have profound implications also for cosmology. No direct experimental evidence does exist today in support of such a theory, nor of the failure of the Standard Model at high energies.

2.1 Standard Model Physics

2.1.1 Heavy Flavour Physics

At LHC large amounts of top and beauty quarks will be produced, even at lower luminosities immediately after the machine is turned on.

It will therefore be possible to do detailed studies of the properties of the top, measuring its mass, m_t, and the branching ratios to various decay modes. The mass enters into radiative corrections, and knowing it will enable more precise calculation of cross sections for various processes. Searches for exotic particles resulting from top decays will also be possible.

In B-physics, the emphasis will be on studying CP-violation in the B_d^0 and B_s^0

systems and determining the angles of the CKM triangle. In addition $B\bar{B}$ mixing, rare B decays and general spectroscopy of systems containg b-quarks will be of interest.

2.1.2 The Higgs Mechanism

In the electroweak theory the mass terms in the lagrangian for the gauge bosons are forbidden by gauge symmetry. Therefore a doublet of complex scalar fields, Φ, the Higgs field, with a potential $V(\Phi) = \mu^2|\Phi^\dagger\Phi| + \lambda|\Phi^\dagger\Phi|^2$, is introduced. Φ couples to the gauge bosons. If $\lambda > 0$ and $\mu^2 < 0$, the minimum of the potential will not be at zero, but rather a continuum of states with $|\Phi| = -\mu^2/2\lambda$, i.e. Φ will acquire a vacuum expectation value, and spontaneously break the symmetry. This will give rise to a dynamical mass term for $W^\pm$ and Z, but leave the photon massless. Of the four degrees of freedom of the original field, one remains that will manifest itself as a scalar physical particle, the Higgs boson H. The mass of this new boson is not predicted by theory.

The Higgs field also couples through Yukawa couplings to the fermions to give them mass. However, the coupling constants must be put in by hand, separately for each fermion, and are also free parameters of the theory.

Direct searches at LEP have excluded a Higgs boson with a mass below 65 GeV[8, 9]. At LEP2 it will be possible, assuming the Higgs is not found, to push this limit to approximately 90 GeV[10]. If λ grows very large, the Higgs becomes very heavy, and the theory becomes strongly interacting, meaning that perturbation theory is no longer valid. Theoretical arguments along those lines indicate that the Higgs cannot be much heavier than 1 TeV, or else some other, hitherto unknown, physics must appear at that scale.

If the Higgs exists and is not previously found at LEP2, it will almost certainly be found at LHC.

2.2 Beyond the Standard Model

Even though it is very successful, the Standard Model is theoretically unsatisfactory in several ways[11, 12]. If one tries to extend the validity of the SM to very high energy scales, the radiative corrections to the Higgs mass tend to drive it to this very high mass scale, while for other considerations, Higgs should have a mass of the order of 0.1–1 TeV. To cancel these radiative corrections and get a Higgs mass in the desired range would require that the parameters of the high energy theory are fine tuned to 34 orders of magnitude. This is commonly referred to as the hierarchy problem. Also, the structure of the Standard Model, with three families and two different theories for their interactions suggests that it is not a fundamental theory. It would be tempting to construct a larger theory

of which the electroweak and strong interactions are low energy manifestations, a so called grand unified theory.

The basic idea is that the gauge interactions of the Standard Model are described by a simple gauge group, which contains the Standard Model $SU_3 \otimes SU_2 \otimes U_1$ as a subgroup and low energy manifestation. This simple gauge group would contain one coupling constant g_X, while the strong, weak and electromagnetic couplings have different numerical values. In a quantum field theory, the coupling constants depend on the energy scale they are probed at, as a consequence of the exchange of the virtual particles surrounding the charge. This is much in analogy with the way a charged particle polarizes a dielectric, reducing the apparent charge at a distance. The electric charge shields, that is, decreases with increasing distance (decreasing energy), while the weak and strong couplings anti-shield. At large distances the strong coupling is much stronger than the weak and electromagnetic couplings. Thus, as we evolve the coupling constants towards high energy, they come together, however not at a single point.

2.2.1 Supersymmetry

Supersymmetry is a symmetry which transforms fermions into bosons, and vice versa (a good review is [13]). Invariance under supersymmetric transformations implies that particles in a supermultiplet are degenerate in mass. It can be shown that the contribution to m_H^2 proportional to the cutoff scale of the theory coming from a bosonic loop is exactly cancelled by a fermionic loop. Since the Higgs mass dependence on the energy scale disappears, the scale of the validity of the theory can be extended without provoking a hierarchy problem. However, no superpartners to known particles are known. It is therefore evident that supersymmetry is not an exact symmetry of nature, but is broken. It is possible to break supersymmetry in such a way so as to preserve the cancellation of the [quadratic] divergences mentioned above. The scale of this breaking cannot be much larger than 1 TeV, if it is still to solve the hierarchy problem. If supersymmetry exists, we thus expect to find new particles at the TeV scale.

Supersymmetry would also alter the evolution of the coupling constants, making it possible for them to meet in a single point. If supersymmetry is further promoted to a local symmetry, it naturally involves gravity, which makes it very attractive for the complete unification of the forces. This connection could also be what sets the scale of supersymmetry breaking.

Supersymmetry requires two Higgs doublets. Of the eight degrees of freedom, three are eaten by the electroweak symmetry breaking, giving mass to $W^\pm$ and Z, as in the SM. Five degrees remain, giving rise to physical particles, two neutral CP-even scalars (h, H), one neutral CP-odd scalar (A) and one charged scalar ($H^\pm$).

The most important feature of supersymmetry phenomenology is the existence of a discrete symmetry, R-parity, which distinguishes ordinary particles from their supersymmetric partners. This symmetry is not predicted by theory, but generally assumed, since it would otherwise imply that lepton and baryon numbers are not conserved. If R-parity is conserved, then supersymmetric particles would be produced in pairs, and their decays would always include an odd number of supersymmetric particles (one or more). The lightest supersymmetric particle (LSP), in most models the neutralino, χ^0, is then stable. Such a heavy neutral particle could contribute to the dark matter of the universe. In a collider experiment this particle would behave like a heavy neutrino, escaping the detector unseen, leaving unbalanced momentum and missing energy in the event. Precise measurement of missing transverse energy is thus essential at LHC.

3. The Vehicles of Discovery

3.1   The Large Hadron Collider

The Large Hadron Collider, LHC, is a proton-proton collider to be built at CERN, with a centre-of-mass energy of 14 TeV and a design luminosity of $10^{34}\,\mathrm{cm^{-2}s^{-1}}$.

LHC [14, 15] will be built in the existing LEP tunnel, measuring 27 km in circumference. LHC will collide protons on protons and thus require the two colliding beams to be accelerated in separate beam pipes. A novel solution using a twin bore magnet consisting of two coils and beam channels housed in a common yoke and cryostat has been chosen, reducing the cost substantially over having separate rings.

The energy available is mainly limited by the strength of the bending magnets. The radius being fixed by the tunnel, LHC needs a bending field of 8.36 T, delivered by 1232 14.2 m superconducting dipole magnets operating at 1.9 K. The cryogenics are based on superfluid helium at atmospheric pressure. Parts of the cooling system from LEP2 will be reused to refrigerate the LHC helium.

The RF accelerating system consists of eight 400.8 MHz superconducting cavities per beam. The beams will be given extra separation at the RF system so that separate cavities can be used. The stored beam energy will be 334 MJ.

There will be two general purpose pp collider experiments, ATLAS and CMS, built according to slightly complementary principles; in addition there will be one dedicated heavy ion experiment, ALICE, and possibly one or several dedicated experiments for B-physics studies.

3.2   Atlas

ATLAS is a general purpose pp collider experiment, meaning that it aims at exploring the widest possible range of new physics, to exploit the full discovery potential of LHC.

The LHC offers a large range of physics opportunities, among which the origin of mass of the elementary particles is a major focus of interest for ATLAS. The detector optimization is therefore guided by physics issues such as sensitivity to

the largest possible Higgs mass range. Other important goals are searches for heavy W- and Z-like objects, for supersymmetric particles, for compositeness of the fundamental fermions, as well as studies of CP-violation in B-systems. At LHC will also be the first opportunity to do high statistics studies of the top quark. The ability to cope well with a broad variety of possible physics processes is expected to maximize the detector's potential for the discovery of new, unexpected, physics.

Many of the interesting physics questions at the LHC have very small cross-sections and thus require high luminosity. The detector has to be able to operate efficiently at these high rates. This puts very special demands on the read-out electronics, and the subsequent data processing.
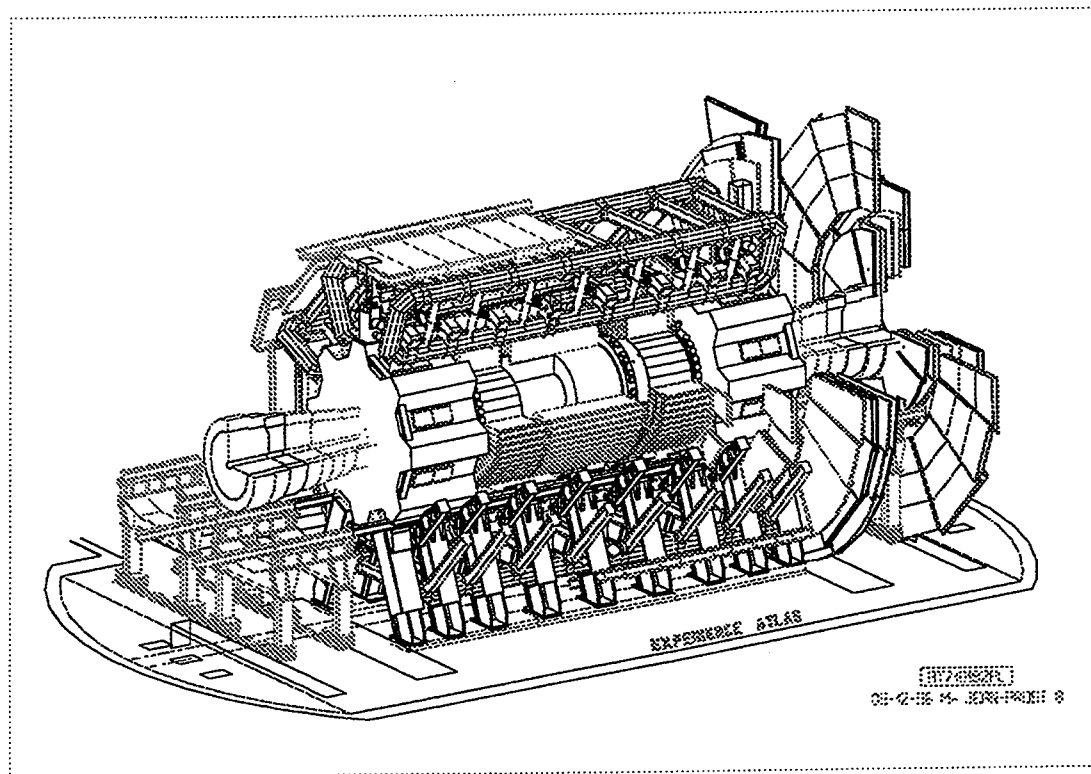

Figure 3.1: A cut out view of the ATLAS experiment.

The ATLAS collaboration has chosen a design which comprises very good electromagnetic calorimetry, complemented by jet and missing transverse energy calorimetry with good hermeticity, efficient tracking and vertexing at high energies and a stand-alone precision muon spectrometer. Fig. 3.1 gives an overview of the experiment.
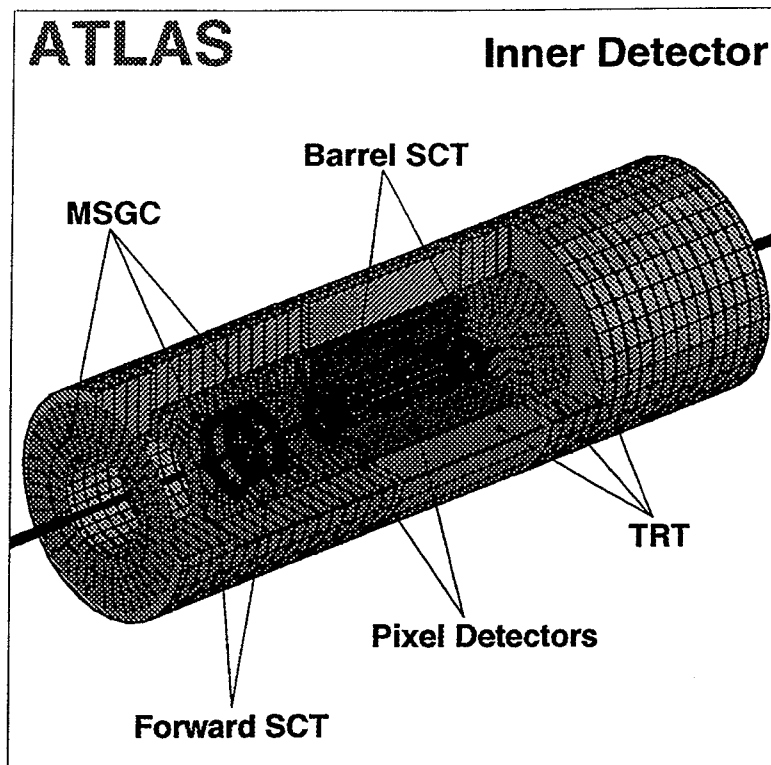
Figure 3.2: The Inner Detector

3.2.1 Inner Detector

The inner detector is shown in Fig. 3.2. Closest to the beampipe there are two barrel shells and eight discs of pixel detectors. Outside of this small-angle stereo strip detectors are used. In the barrel region silicon is foreseen while in the high flux forward parts radiation hard GaAs substrates are used. For the forward system large area silicon microstrip detectors have been developped ("wheels"). Together these detectors are referred to as the "Semi-Conductor Tracker". Outside of it the track density is lower and straw tubes are used for tracking. These are embedded in a radiator foam generating X-ray transition radiation, giving electron identification ability independent of the calorimeter. This detector is called the "Transition Radiation Tracker". The inner detector occupies a cavity of radius 115 cm and length ±345 cm inside the 2 T superconducting solenoid.

3.2.2 Calorimetry

Figure 3.3 shows a drawing of the ATLAS calorimeter system. The structure is divided into a barrel and two end-cap parts. The central cryostat houses the liquid argon (lead absorber) electromagnetic calorimeter and the superconducting
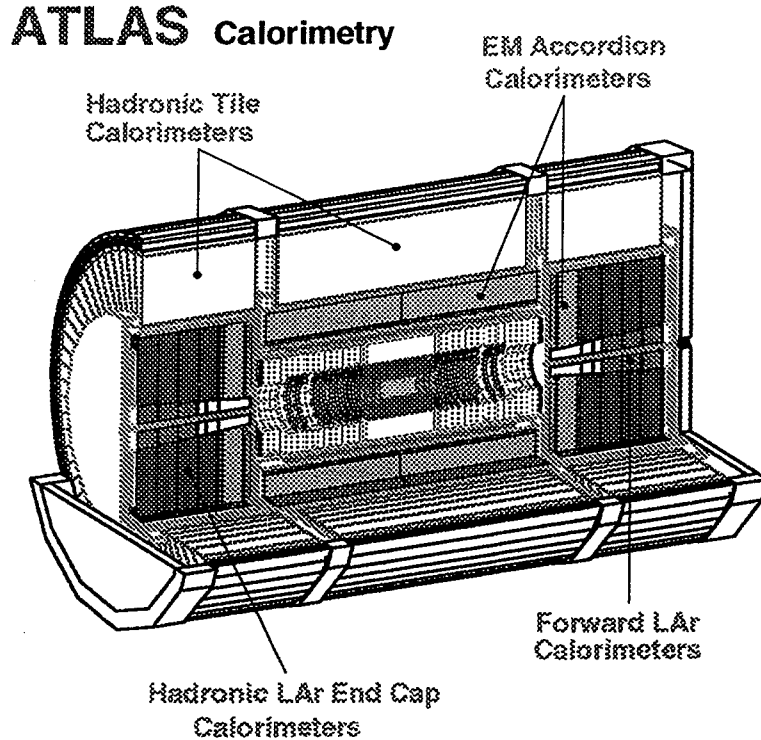
Figure 3.3: A cut out view of the ATLAS calorimetry system.

solenoid. In each end-cap there is an additional cryostat containing the liquid argon end-cap electromagnetic and hadronic calorimeters, as well as the forward calorimeter (also of LAr type, but tungsten absorber).

The hadronic calorimetry in the barrel region is provided by a novel-design scintillating tile calorimeter consisting of a large barrel part, flanked by two extended barrels, covering $|\eta|$ up to 1.5 (pseudorapidity,$\eta = -\ln\tan\theta/2$ is a convenient (angular) measure in which the distribution of decay products is approximately invariant of the boost of the decaying system). The Tilecal is further discussed in Chap. 5. The calorimeter support structure is also used as flux return for the solenoidal magnetic field. The entire calorimeter system allows for hermetic coverage in the pseudorapidity range $|\eta| \leq 5$.

3.2.3 Muon Chamber System

The calorimeter system is surrounded by a huge muon spectrometer. A superconducting air core toroid provides a large field volume and a strong bending power without introducing much material thus reducing multiple scattering effects. The air core toroid consists of eight coils in the barrel part, each 26 m long, going between the radii of 4.7 and 9.75 m and housed in separate cryostats. The end-cap

coils, eight on each side, share a common cryostat.

The muon system consists of three measurement stations; one at the inner limit of the magnetic volume, one at the middle, and one at the outer limit. The barrel and part of the end-cap will be equipped with monitored drift tube chambers, which consist of two layers of three or four planes of pressurized thin wall drift tubes. For the rest, cathode strip chambers are considered. Separate chambers are used for triggering.
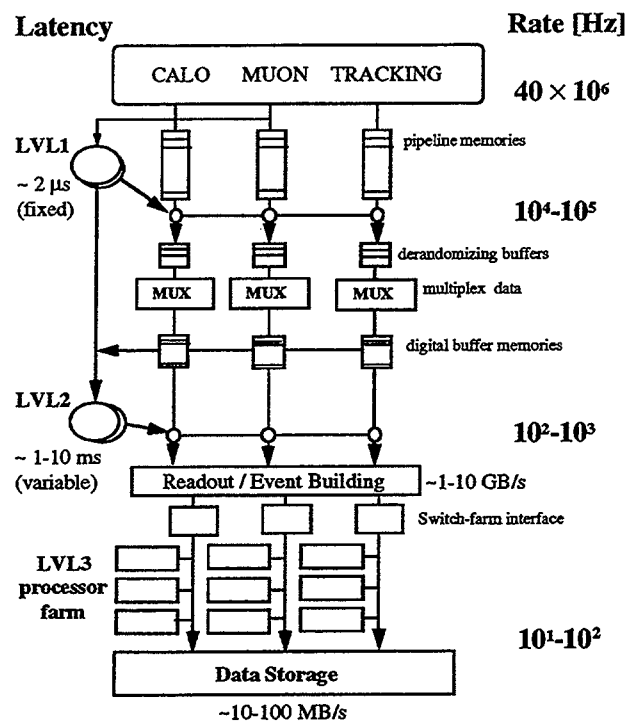
3.2.4 Trigger

Figure 3.4: The ATLAS three level trigger architecture.

The ATLAS trigger is organized in three levels, as shown in Fig. 3.4. At level 1 special purpose processors act on reduced granularity data from a subset of the detectors. The level 2 triggers uses full granularity, full precision data from most of the detectors, but examines only regions of the detectors pointed out by level 1 as containing interesting data. At level 3, the full event data are used to make the final selection of events to be recorded for offline analysis.

L1 accepts data at the full LHC bunch crossing rate of 40 MHz, reducing it to 100 kHz, which is the acceptable input rate to L2. The latency of L1 is fixed, about 2 μs. During the processing, data from all parts of ATLAS are held in pipeline

memories. The muon system and the calorimeter have separate L1 processors; the data from the inner detector is too complex to use in a L1 trigger.

L2 reduces the rate from 100 kHz to about 1 kHz with a variable latency of the order of 1 ms. The information from the L1 system is used to identify regions of the detector containing interesting features such as high-p_T e.m. clusters, jets and muons. The L2 then only has to process information in those regions with the corresponding advantages in terms of required processing power.

After an event is accepted by L2 it is sent to L3 which can do a full global event reconstruction with latencies of up to 1 s.

3.2.5   Overall Measure

The overall size of ATLAS will be 22 m in height times 26 m in length for the toroid coils. The forward muon chambers are located 21 m from the interaction point. The overall weight of ATLAS is some 7000 tons.

4. Hadron Calorimetry

A calorimeter is a device in which the incident particle is caused to interact with the medium and subsequently deposit all its energy inside it. The degradation of the incoming particle's energy goes through the development of a shower of particles with increasingly lower energy. A very tiny fraction of this energy appears in a form that can be measured, e.g. scintillation light, Čerenkov radiation or ionization, whereas most of the energy is dissipated in the form of heat.

The calorimeter measures the energy of particles. The quality of this measurement is indicated by the intrinsic resolution of the energy measurement and the linearity of the calorimeter signal with respect to the incident energy. For hadronic calorimetry obtaining linear response is a non-trivial issue.

4.1 The Physics of Hadron Showers

The physics of electromagnetic showers is rather simple with a few well understood processes governing the evolution of the shower. This makes the description of electromagnetic showers fairly simple. Hadronic showers, on the other hand, are quite complicated, with a much wider variety of processes that can occur at all stages of the shower development. As a result, they are harder to model in detail and the Monte Carlo models must be tuned using experimental data.

Hadron showers develop through a series of interactions when a strongly interacting particle, a hadron, enters a dense medium. From each interaction a host of particles emerge which may themselves continue the chain and produce new particles through subsequent interactions or truncate it by being absorbed into the calorimeter. Unlike the electromagnetic shower, where most of the energy appears in the form of detectable ionization energy, a hadronic shower loses about 50% of its energy in nuclear excitations, breakup of nuclei and evaporation of protons and neutrons. Nuclear deexcitations and secondary π^0s produce photons, and thus part of the shower is electromagnetic in character.

4.1.1 Electromagnetic Sub-showers

During the shower development, γs, ηs and π^0s are produced, which propagate the shower electromagnetically without any further nuclear interaction. They

constitute the electromagnetical part of the hadronic shower. They tend to initate well localized electromagnetic showers in the calorimeter.

The fraction of the incident energy that is converted into π^0s (the dominant electromagnetic component) has big fluctuations from event to event and is dominated by the π^0 production in the first interaction. On average, one third of the mesons produced in the first interaction are π^0s. The remaining charged pions, if sufficiently energetic, can produce π^0s in subsequent interactions, and so forth. The higher the incident particle energy, the more collisions on the average, and the more opportunities to convert energy to electromagnetic. Thus the electromagnetic fraction increases with energy.

The particles participating in the electromagnetic shower lose energy to the calorimeter medium primarily by ionization and, for positrons also annihilation. When the photon energy falls below the critical energy, about 1 MeV, the dominant processes become Compton scattering and the photoelectric effect, thus truncating the shower.

4.1.2 The Purely Hadronic Part

If an incoming high-energy hadron strikes an atomic nucleus, the most likely process to occur is spallation. We can distinguish two stages in this process:

- The development of a fast intranuclear cascade within a time interval of 10^{-22} sec. When a high-energy hadron enters matter, it will defy the coulomb field of the atom and engage in quasi-free collisions with nucleons within the nucleus. Nucleons so struck may hit other nucleons inside the nucleus. In this process, fast protons, neutrons and heavy nuclear fragments, like αs may be created, apart from pions. These may either be caught by the nuclear barrier or escape to strike other nuclei. In either case, the nucleus (or fragment thereof) is left in an excited state.

- The shower evaporation step, in which the intermediate nuclei resulting form the preceding step deexcite. Nucleons (thermal neutrons, protons, αs) and γs from nuclear transitions are emitted in successive evaporation steps. This happens on a timescale of 10^{-18} s. Heavy nuclei may also fission.

Fission only happens for very heavy elements, and is certainly unimportant for iron. It can either occur as part of spallation processes or as part of the energy loss mechanism of the abundant thermal neutrons produced in nuclear interactions.

In the hadronic shower development, a large amount of photons from nuclear processes is produced. Excited nuclear fragments from spallation and fission predominantly decay back to their ground states by means of γ-emission. Soft evaporation neutrons also produce gammas when they scatter inelastically on other nuclei. The vast majority of these have an energy of the order of an MeV.

Due to binding energies and nuclear breakup, a sizable fraction of the available energy is absorbed, leading to a reduction of the signal. In addition, neutrinos leave the detector undetected, also contributing to the signal loss. Muons are essentially minimum ionizing particles and leave only very small part of their energy in the detector, further degrading the signal resolution.

4.1.3 The Sampling Fraction

The response from the calorimeter is dependent on the type of the incident particle. The signal is determined by two factors:

- The amount of ionization deposited in the active layers.

- The ionization density of the active layers.

To compare signals of different particle types in the calorimeter, we compare their sampling fraction, defined as the ratio of the detected energy to the total deposited energy in the calorimeter.

The sampling fraction of a m.i.p., a minimum ionizing particle, sets the scale for the calorimeter signal. A m.i.p. is an imaginary particle which loses energy only by ionization and whose energy loss per unit length is equal to the minimum value of the material concerned. The energy deposited by a m.i.p. depends mainly on the thickness of the material and only weakly on the material itself. Typical sampling fractions for calorimeters with plastic scintillator read-out are about 2–10%.

The ratio between the sampling fraction for a specific particle type i, S_i, to that of a m.i.p. $S_{\mathrm{m.i.p.}}$, is refered to as the sampling ratio, i/mip.

4.2 The e/h ratio

Due to the large fraction of the energy lost in nuclear breakup, the efficency for detecting the hadronic part of the cascade, ε_h, is usually smaller than the efficiency for detecting the electromagnetic part, ε_e. The calorimeter response to the full shower is then:

$$R = \varepsilon_h E_h + \varepsilon_e E_e,$$

where E_h and E_e is the energy of the hadronic and electromagnetic part of the shower respectively.

For events with a large electromagnetic fraction ($E_e \gg E_h$, 'type E events') the overall detection efficiency is better and the shape of the energy distribution will be sharp and resemble that of electrons of an equivalent energy. For 'type H events' ($E_h \gg E_e$) the detection efficiency is worse and the width of the distribution broader. Hadron showers can range between these two cases. The larger the difference between ε_e and ε_h, the broader the convoluted distribution

will be. A calorimeter for which $\varepsilon_e \approx \varepsilon_h$ minimizes the energy spread due to fluctuations in the number of initial π^0s, and is referred to as compensating. The two cases are depicted in Figure 4.1.
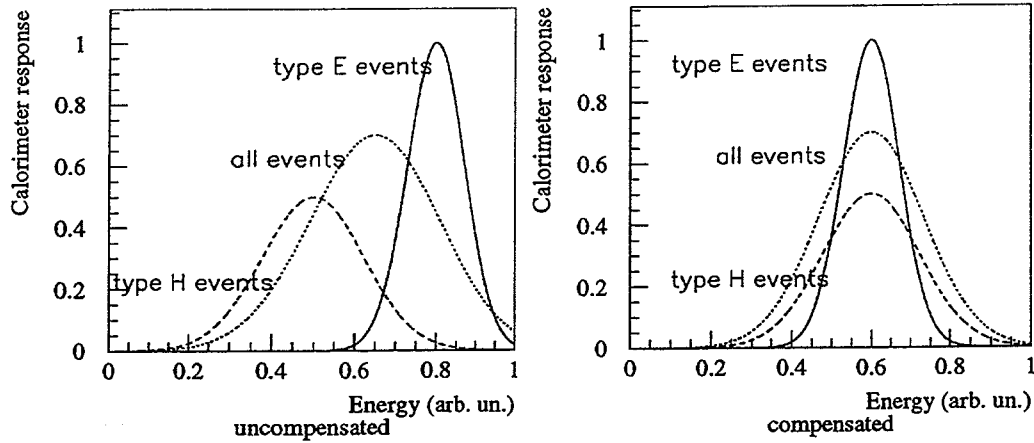

Figure 4.1: The effects of non-compensation.

The ratio between the response for electrons of a certain energy and pions of the same energy is referred to as e/π:

$$\begin{aligned} e/\pi(E) &= \frac{\varepsilon_e E}{\varepsilon_e E_e + \varepsilon_h E_h} \\ &= \frac{\varepsilon_e}{\varepsilon_e \langle f_{\pi^0}(E) \rangle + \varepsilon_h (1 - \langle f_{\pi^0}(E) \rangle)} \\ &= \frac{e/h}{1 + \langle f_{\pi^0}(E) \rangle (e/h - 1)}, \end{aligned}$$

where $\langle f_{\pi^0}(E) \rangle$ is the average electromagnetic fraction in a hadronic cascade, and e/h a shorthand for $\varepsilon_e/\varepsilon_h$.

The relation between e/h and e/π as a function of energy has been investigated by Wigmans [16] and by Groom [17] who for $\langle f_{\pi^0}(E) \rangle$ found logarithmic and power law parametrizations, respectively:

$$\langle f_{\pi^0}(E) \rangle = 0.1 \ln E(\text{GeV}) \qquad \text{(Wigmans)}$$

$$\langle f_{\pi^0}(E) \rangle = 1 - (E/E_0)^{m-1} \qquad \text{(Groom)}$$

Here E_0 is a scale energy at which the cascade would be entirely hadronic, or an effective turn-on energy for π^0 production. E_0 and the exponent m are obtained

from fits to experimental data. Groom gets $E_0 = 1.45$ GeV and $m = 0.801$ for π^+ in iron.

A non-compensating calorimeter thus has worse resolution than a compensating. But also, since the number of π^0s goes slower than linearly with energy, the sampling term contribution to the resolution will not improve as $1/\sqrt{E}$.

It is important to note that the e/h ratio is an intrinsic property of the calorimeter, while the response of electrons compared to pions, e/π, is a function of energy (since $E_e \propto \ln E$). This can be used to deduce e/h for a calorimeter.

In principal, there are two means to achieve compensation: either enhance ε_h or reduce ε_e.

4.3 Sampling Calorimeters

Sampling calorimeters are devices in which the functions of energy degradation and energy measurement are separated in alternating layers of different substances. This implies advantages and disadvantages compared to homogeneous calorimeters, in which the absorber and read-out medium are the same and permeates the full volume of the calorimeter. The obvious advantage is that the passive absorber medium can be chosen separately from the active medium. This implies that the calorimeter can be more specifically tailored to the needs of the experiment: compacter dimensions, higher granularity, better signal uniformity etc. The disadvantage is that only a part of the energy released in the calorimeter that is in principle measurable will make it to the active layers, the remainder being totally absorbed by the passive medium. Thus, the resolution will be further deteriorated from fluctuations in this ratio.

4.3.1 Compensation of Sampling Calorimeters

Sampling calorimeters are the most natural choice if e/h close to unity is desired. In homogeneous calorimeters one can play with the chemical composition of the medium in order to enhance ε_h, mostly by using a hydrogeneous medium to increase the sensitivity to slow neutrons. In sampling calorimeters, there is a number of choices. One obvious, but not so important, effect is that of fission in uranium. It does contribute, but requires a hydrogeneous sampling medium, to absorb the neutrons. More important is the reduction of the response to the electromagnetic part of the shower caused by the juxtaposition of high-Z absorbers and low-Z sampling layers. The underlying physical process is simply the details of the energy loss of the low energy γs and electrons, in particular the Z-dependence for certain electromagnetic processes: the cross-section for ionization goes as Z, pair production as Z^2 and the photo-electric effect as Z^5. Therefore, most of the low energy electrons are produced in the high-Z absorber, and due to

their small range, are also absorbed there. The low energy photons which reach the low-Z active layers are not efficiently sampled.

4.3.2 Energy Resolution of Sampling Hadron Calorimeters

The showering mechanism used in calorimetry is an intrinsically stochastical process. The number of steps involved increase with energy, causing the intrinsic accuracy of the measurement to increase, this in contrast with tracking detectors measuring momentum with the help of a magnetic field. This is a very attractive feature, considering the high energies available at future colliders.

When the shower develops, some fraction of its energy is transformed into a measurable signal, as a result of the energy deposited by charged particles when traversing the active layers. The fluctuations in this process affect the energy resolution.

In addition, because of the non-gaussian fluctuations in the fraction of energy going to π^0 production, the intrinsic non-compensation of the calorimeter, e/h, will play a crucial role.

The read-out mechanism contributes to the resolution through photo-electron statistics, electronic noise, non-linearities (imperfect calibration) and digitization effects.

The general expression for the total energy resolution for the detection of hadronic showers is:

$$\frac{\sigma(E)}{E} = \frac{a}{\sqrt{E}} \oplus b \oplus \frac{c}{E}$$

where a includes contribution from sampling fluctuations, intrinsic shower fluctuations and photostatistics (assuming PMT read-out). The constant term b is due to non-compensation and calibration errors, while c comes from electronics noise. This last term can usually be neglected at high energies.

5. The Tile Calorimeter

5.1 Design Goals

The major goals of the hadronic calorimeter of ATLAS [18] are to identify jets and to measure their energy and direction, to measure the total missing energy and to enhance the particle identification of the electromagnetic calorimeter by measuring leakage and isolation.

This implies as design goal [19] a resolution of $\sigma/E = 50\%/\sqrt{E}\oplus3\%$, a linearity of 1-2 % up to a few TeV and a granularity of $\Delta\eta \times \Delta\phi = 0.1 \times 0.1$. In addition, the hadronic calorimeter should absorb all radiation in front of the muon system (requiring about 11 λ, including electromagnetic calorimeter, solenoid, cryostat and the Tilecal girder) and provide low p_T muon identification.

From simulations the maximum expected energy in a single cell in Tilecal is about 2 TeV at a rate of a few events per year. At the lower end, the calorimeter should be able to measure the signal of a muon depositing 0.5 GeV in the thinnest cell; assuming 15 counts for this signal, we require a dynamic range of 60 000 or 2^{16}.

The resolution of the read-out system should be small compared to the intrinsic resolution of the calorimeter. The latter has been measured to be $\sigma/E = 47\%/\sqrt{E} \oplus 2\%$. Thus, an electronic precision of eight bits everywhere (0.4 %) is adequate. This can be achieved by reducing the signal with a non-linear compression function, as described in Sec. 5.4.

The current status of the project is described in the Technical Design Report [20].

5.2 Principles

The Tile calorimeter is designed as a sampling calorimeter based on iron absorbers and plastic scintillators read out with wavelength shifting fibres. The scintillating tiles are oriented radially, perpendicular to the colliding beams, and hence almost parallell to the direction of the particles impinging on the calorimeter, as shown in Fig. 5.1. The sampling homogeneity is quite good, and is enhanced by the fact that showers tend to start in the electromagnetic calorimeter. This configuration
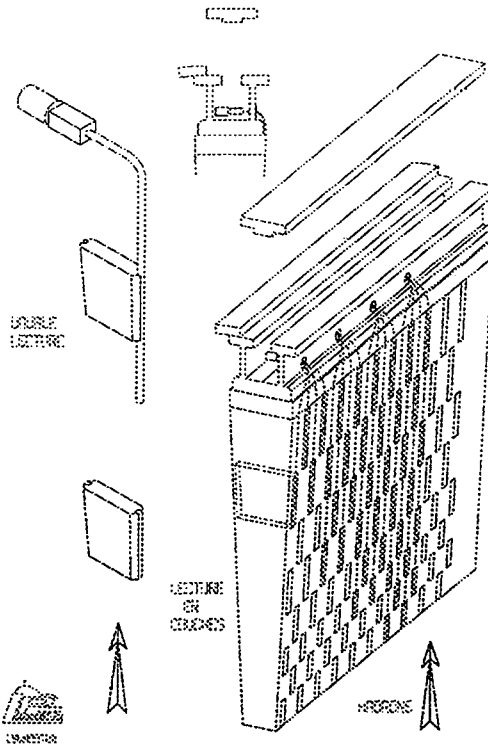
Figure 5.1: Principles of of the Tile calorimeter design.

allows for a simplified read-out geometry with the fibres running radially out along the edges of the scintillating tiles, leaving minimal dead space and making the mechanical construction of the calorimeter self-supporting.

The calorimeter has a cylindrical shape between the radii of 228 and 423 cm (of which 157 cm is instrumented iron). Longitudinally the structure is divided in three sections, a central (the barrel) 564 cm in length, flanked on both sides by the extended barrels, each 264 cm long. The barrel and the extended barrels are separated by gaps of 0.70 m, the crack, required to route the cables from the inner detector and the electromagnetic calorimeter, as well as the cryogenics of the solenoid.

A shorter submodule, the plug, is inserted into the crack to partially compensate for the loss of energy deposition in the crack.

Each part is azimuthally divided in 64 modules; each sector is segmented in three layers having thicknesses of 1.9, 4.2 and 1.5 interaction lengths (λ) going radially outwards. The layers are further segmented in readout cells. This is done by grouping the read-out fibres of several scintillators to a single photomultiplier to achieve a granularity of $\Delta\eta \times \Delta\phi = 0.1 \times 0.1$ (0.2×0.1 for the outermost layer).
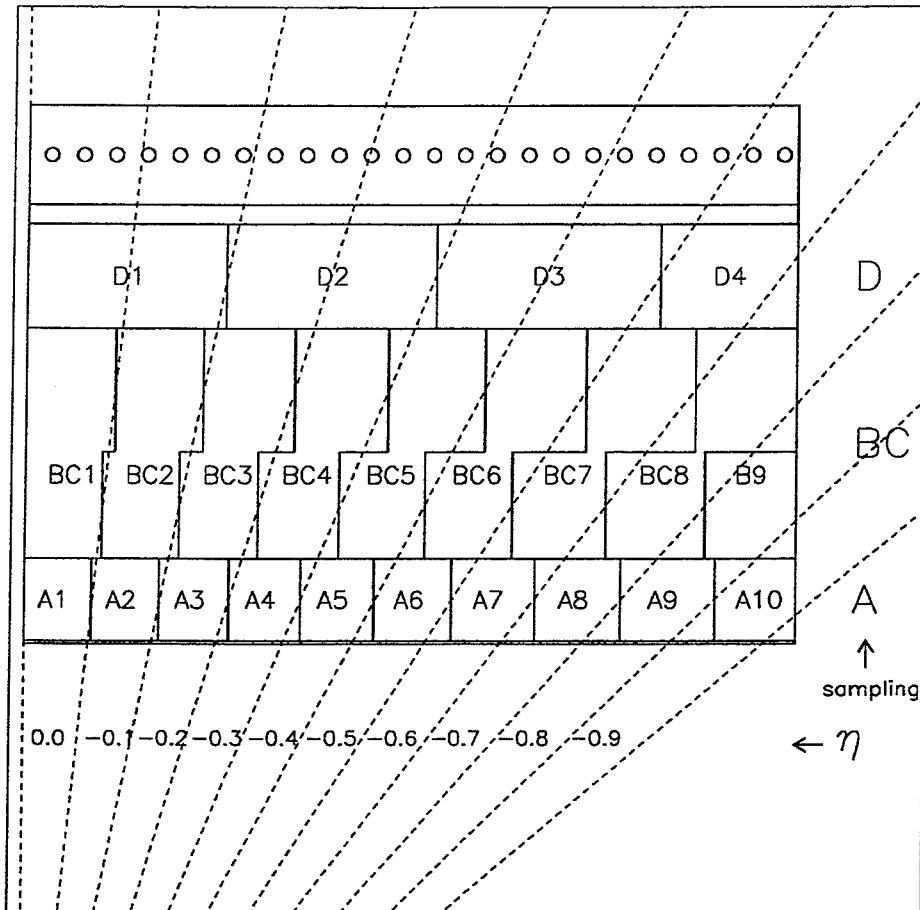
Figure 5.2: Cell geometry of half of a barrel module. The fibres of each edge of each cell are routed to one PMT. The PMTs are indicated by circles.

The read-out geometry of a barrel module i shown in Fig. 5.2; the extended barrel is done similarly.

Each module is built by a stack of repeating elements (periods). As shown in Fig. 5.3 each period is a stack of four layers. The first and the third layers are formed by large trapezoidal steel plates (master plates), 5 mm thick and spanning the entire radial dimension of the module. In the second and fourth layer, smaller trapezoidal plates (spacers) and scintillators alternate along the radial direction. The spacer plates are 4 mm thick and of 11 different sizes. The spacers are glued to the masters with epoxy.

The scintillating tiles, 3 mm thick, are inserted into the module after the mechanical steel assembly. The further out a tile is, the larger it is, lowering the light yield because of attenuation in the tile; this effect cancels quite nicely against the shorter fiber lengths required.
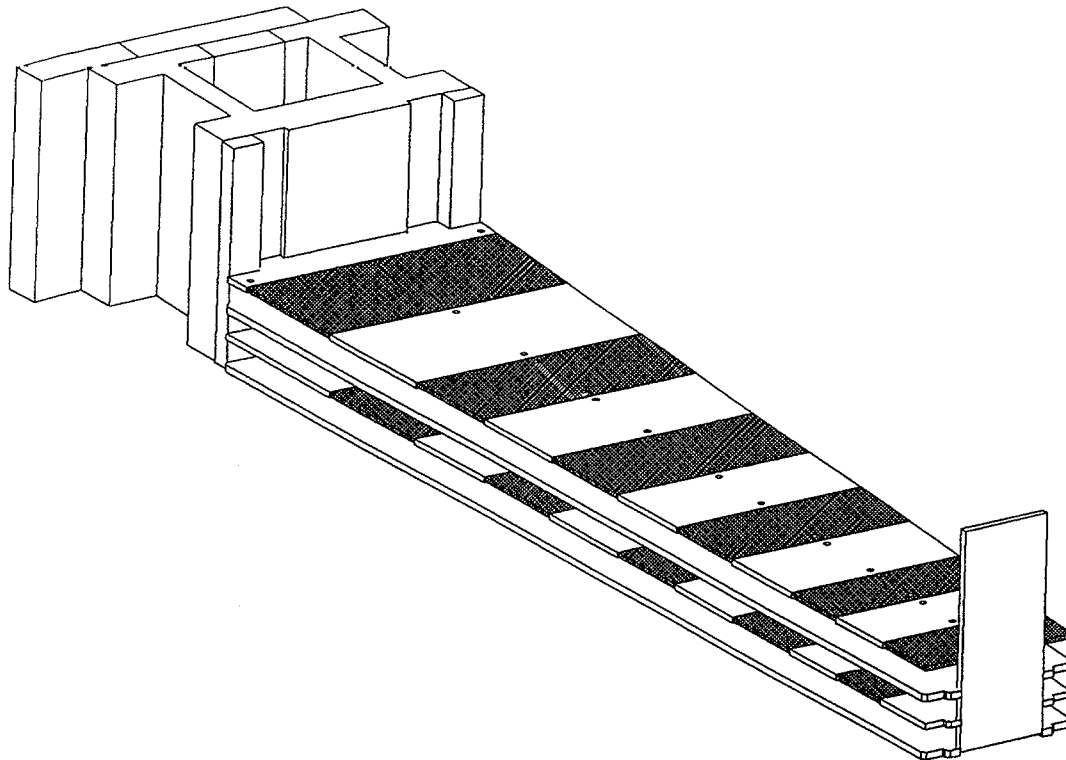
Figure 5.3: Exploded view of one period of a Tile Calorimeter submodule.

The iron to scintillator ratio is 4.67:1 by volume, making the calorimeter non-compensating [21], but offline data treatment can correct this.

There are two holes penetrating each spacer, each scintillator, and, in the corresponding places, the master plates. These are used for positioning the tiles, and for calibration. Mechanical stability comes from a 10 mm front plate at the inner radius and a rigid girder, also housing the PM tubes and readout electronics and doubling as flux return for the solenoid, at the outer.

5.3   Read-Out

The wavelength shifting fibers run along the sides of the modules and are grouped into bundles at the outer end of the detector. The bundles are then routed through rubber feedthroughs in the side of the girder to a light mixer which spreads the light evenly over the photomultiplier tube surface. Inside the base of the PMTs sits a voltage divider and the 3-in-1 card (see Fig. 5.5). The 3-in-1 card is a two part card, with the analog part piggybacking the digital, providing three functions: It contains a fast unipolar shaper, a compressor limiting the dynamic range of the signal to 10 bits and calibration circuits, including the charge injection and an
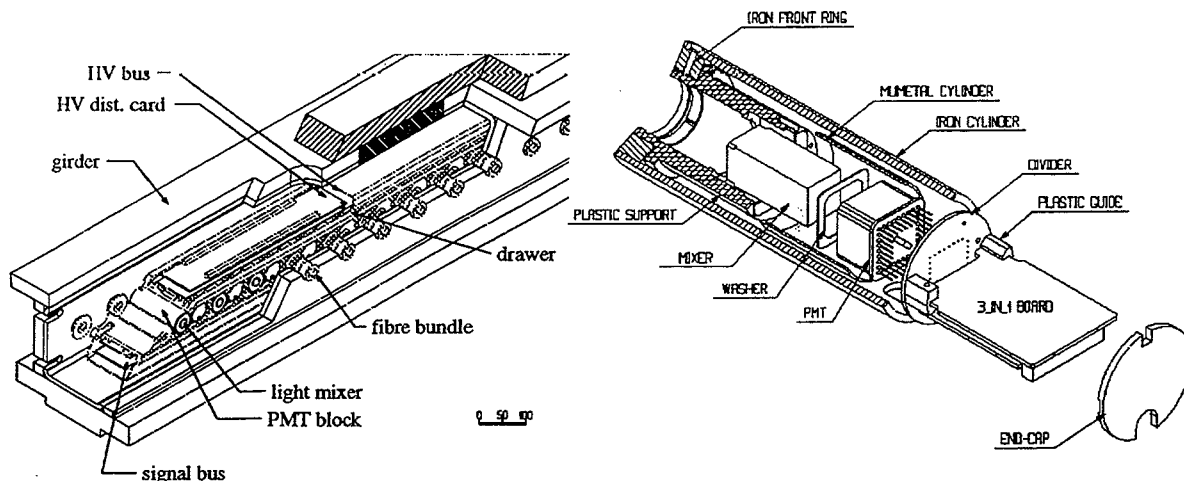
Figure 5.4: Cut out view of drawer.

Figure 5.5: Components of the PMT-block.

integrator for the source scan.

The light mixer, the PMTs, the voltage divider and 3-in-1 card are housed inside a soft iron and mu-metal housing, shielding against stray magnetic field from the toroid. The PMT blocks are mounted inside drawers (see Fig. 5.4) in the girder, 24 in each drawer, of which two make a super drawer. The barrel modules take two super-drawers, and the extended barrel modules one. Inside each drawer the control signals to the 3-in-1 boards are distributed along mother boards (70 cm long, connected in series) and the high voltage along 140 cm long bus boards.

The drawers can be retracted for service.

5.4 Read-Out Electronics

The fast read-out electronics must process signals from 11 110 photo-multipliers every 25 ns. As described above, these signals have a dynamic range of 16 bits and a precision of 10 bits. Signals corresponding to the energy in the 2000 calorimeter trigger towers must be formed and sent off to the level 1 trigger electronics on every beam crossing. During the 2.5 μs latency of the level 1 trigger, the individual calorimeter trigger signals are stored. Following the latency period, data from events accepted by the level 1 trigger are passed to read-out driver modules for further processing prior to transmission to the level 2 trigger. Signals from beam crossings failing level 1 are discarded.

The read-out electronics are divided into several parts. The front-end electronics are located on the 3-in-1 cards within the PMT blocks as described above. Here the current pulse from the PMT is shaped and converted into a voltage signal which is compressed and then transmitted by short shielded cables to the fast digitizers located at one end of the super-drawers.

5.4.1 Front-End Electronics

In the baseline configuration a design based on the FERMI concept is used.

The **shaper** [22] is a linear circuit designed to process the current pulse from the photo-multiplier tubes into analog unipolar signals. With an output swing of 4 V differential, an output noise level of less than 60 μV is required to preserve the 16-bit dynamic range. The shaper is designed as a four-pole low pass Bessel filter. The shaper output is a unipolar pulse of 50 ns FWHM with amplitude proportional to the input charge (see Fig. 5.9).

The transfer function of the **compressor** is designed to have a piece-wise linear form with four segments. The output of the shaper is connected to four differential stages with different gains, and the output is subsequently summed. The principal is shown in Fig. 5.6.
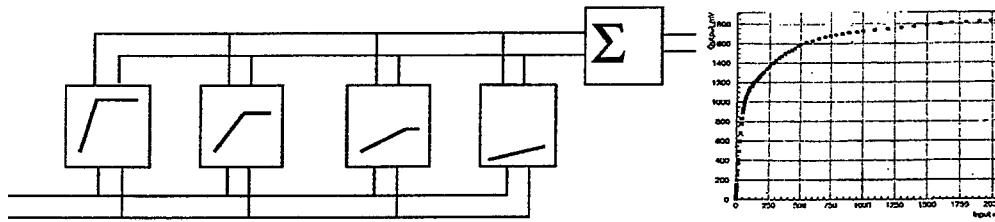

Figure 5.6: Concept of the compressor. The compressor is a current sum of four linear amplifiers with gains approximately 18.5, 1.3, 0.14 and 0.09 and upper cutoffs on the input voltage of 60, 470 and 1200 mV respectively. The fourth amplifier spans the full 2000 mV input range of the compressor. To the right, a typical transfer function as measured in laboratory.

As an option, investigations are also conducted on a solution with two linear outputs with gains differing by a factor of 32. The outputs would be digitized separate ADCs with a dynamic range of twelve bits.

5.5 Calibration

Three calibration systems are provided for different parts of the readout:

- A Cesium source calibration for intercalibration of the individual cells.

- A laser calibration system for monitoring the long term stability of the PMTs and associated electronics.

- A charge injection system for precise calibration of the read-out electronics.
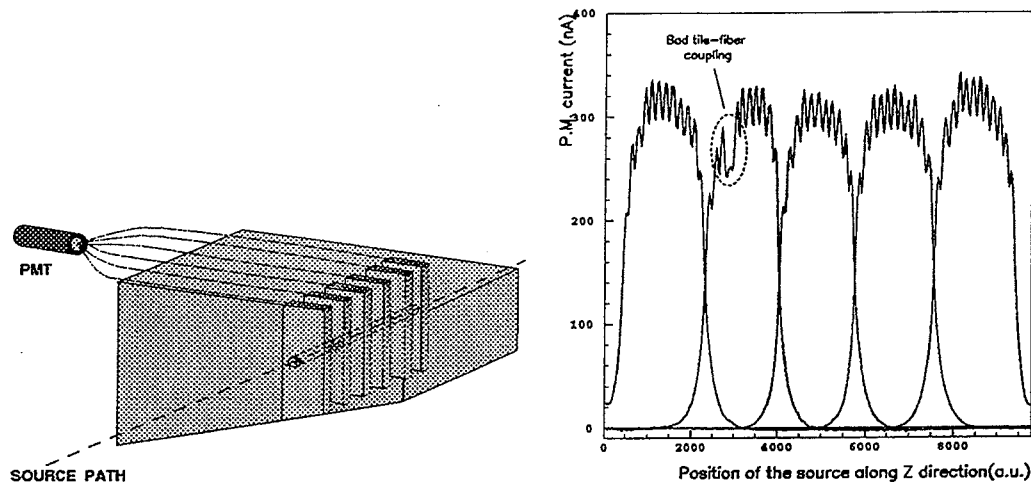
5.5.1 The Cs Calibration System

Figure 5.7: Principles of the Cs calibra- Figure 5.8: Example of z-scan with Cs
tion system.   source.

The Tile Calorimeter is designed to allow a movable radioactive source to pass through every scintillator tile. Each scintillator tile has two holes along the symmetry axis; the source guide tube is inserted through one. The concept is schematically shown in Figure 5.7. The movable γ source is used to:

- check the quality of the optical response and its uniformity.

- equalize the response of all read-out cells, by adjusting the HV of the corresponding PMT to obtain the same average current from each cell.

- monitor in time the average current of each cell, by running the source periodically. As the average current for each cell is proportional to the overall signal, monitoring it allows the overall energy calibration to be maintained.

A movable source system allows the use of just a few sources to calibrate the whole Tile Calorimeter. For long-term monitoring of the calorimeter response, the precisely known decay rate of the sources is necessary.

In Figure 5.8, from the first Tile Calorimeter publication[23], the current induced in five PMTs (reading out five consecutive calorimeter cells) is shown as a function of the source position. The multiple peak structure in the response of each PMT is due to the passage of a 5 mCi ^{137}Cs source through individual tiles; a case of faulty light collection from one tile is clearly seen. The capability to see individual

tiles is due to the short mean free path of the ^{137}Cs gammas, which is of the order of the 18 mm separation between tiles.

5.5.2 The Laser Calibration System

The main purpose of the laser system is to monitor the response of the PMTs on any desired time scale, from the very shortest (minutes) to the duration of ATLAS. It is planned to obtain the PMT gain to a relative precision of 0.5% by measuring the laser light intensity pulse by pulse. This system will also be useful to check the pulse electronics following the PMTs.

The core of this system is a frequency-doubled YLF solid-state laser in which the light pulses are externally triggered and intensity-modulated; the system is fully computer controlled. The laser pulses closely mimic the scintillating light produced by particles in the calorimeter, having a wavelength of 480 nm and a pulse width of about 15 ns.

The laser pulse intensity is precisely measured on a pulse-by-pulse basis by photodiodes. The linearity of the photodiode read-out electronics is checked with a charge injection system; the response of the photodiodes is monitored with an ^{241}Am alpha source, which provides a reference which is stable in time and insensitive to environmental changes.

Laser calibrations are performed generating a train of pulses of increasing amplitude, reaching the upper end of the PMT dynamic range. The light is transmitted to the PMTs through clear fibres. The effective dynamic range of the laser in this mode is only about 30, whereas the calorimeter dynamic range in ATLAS is about 60000. To obtain this range a set of remotely controlled filters will be installed on the laser light path. Amplitude monitoring and timing measurements are made downstream of these filters.

In the test beam, the laser system is used to continuously monitor the calorimeter PMTs. It plays several roles:

- fast on-line controls of the operation of the PMTs and the associated front-end electronics,

- measurements of the drift of the PMT relative gains,

- measurement of the linearity of each PMT,

- other test and diagnostic functions, such as finding cabling errors, measuring cross-talk and calorimeter photoelectron statistics.

5.5.3 The Charge Injection System

It is important to calibrate the behaviour of each read-out channel over its full dynamic range. This permits a prompt diagnosis of read-out faults, a test for

cross-talk effects, and tests with realistic patterns of energy deposition over the full calorimeter. Each 3-in-1 card has circuitry to permit this and the system is controlled through the mother boards by external VME modules connected to the ATLAS detector control system (DCS).

To provide a 16-bit dynamic range with modest resolution and cost, each 3-in-1 card is equipped with a pair of 8-bit DACs connected in series. The DACs, supplied by a precise external reference voltage common to the entire drawer, charge a 1% precision capacitor at the input to the pulse shaper. On command from the control logic, one end of the capacitor is shorted to ground through a CMOS switch to discharge the capacitor through the shaper.
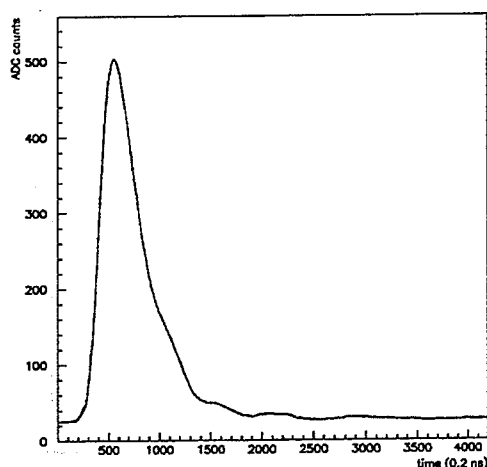
Figure 5.9: Shape of charge injection pulse (20.2 pC)
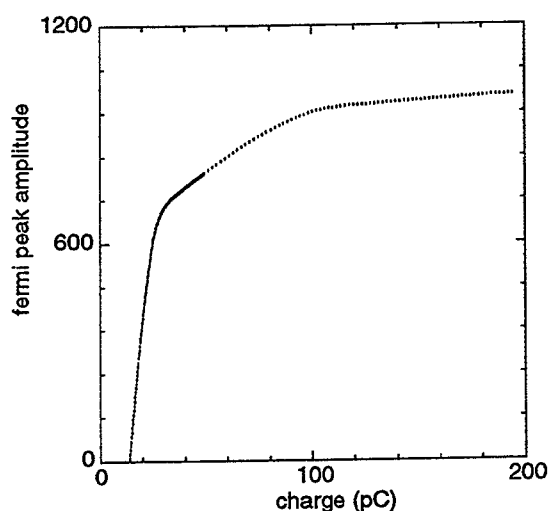
Figure 5.10: Charge injection test of the shaper-compressor stage.

The timing of the pulse injected with respect to the digitizing clock can be controlled with a 0.2 ns step. Fig. 5.9 shows the pulse shape scanned by varying the timing in this way. Figure 5.10 shows the overall transfer function of a read-out channel measured with this system. The various ranges of the compressor are evident.

5.6 Testbeam Programme

The Tile Calorimeter test beam programme was started in 1993, as CERN R&D programme RD34[24]. Since then it has grown into a major ATLAS effort, drawing a lot from collaboration with other ATLAS subdetectors, mainly the Liquid Argon Calorimeter.

Up to now three different types of setups have been used:

- Standalone measurements with reduced scale prototypes (cf. Chapter 6),

- Combined measurements with the LAr electromagnetic prototype and Tile Calorimeter prototype modules [25] and

- Full scale barrel sector (Module 0) in standalone measurements.

Early measurements were performed in the H2 beam line at the SPS at CERN, while for later measurements the H8 beam line was used. The beam lines were instrumented in a standard fashion with one threshold Cherenkov counter used for π/e separation for $E \leq 20$ GeV, a pair of delay-line wire chambers for both x and y coordinates, and scintillators to define a trigger. The scintillators defined a beam spot of around 2-3 cm, while the chambers allowed the reconstruction of the impact point on the calorimeter face to better than ± 1 mm. Data were taken with muons, pions and electrons between 10 and 400 GeV. The momentum bite of the H8 beam, $\Delta p/p$, was always less than 0.5%. Recorded event rates were about 150 per burst.

In this thesis, work from the standalone testbeam in 1995 with the one meter prototypes is presented.

6. Testbeam 95 — Prototypes

In July 1995 a stack of five prototypes of the ATLAS Tilecal, described below, was tested in beam at the CERN SPS. Module 3, the central module in the stack, was equipped with active splitters and double sets of read-out electronics for each channel, one based on a standard integrating 12-bit ADC, and one based on the FERMI concept with a prototype compressor and a sampling ADC.

The aim of this study was to compare the FERMI compressor and sampling ADC with a conventional integrating ADC in order to evaluate the performance of the FERMI concept. We therefore concentrate our analysis on the highest energy pion runs taken, in order to minimize the contributions from intrinsic and sampling fluctuations. In this way we can compare the contribution to the constant term from FERMI and standard electronics.

As this work is the subject of the enclosed paper, to be submitted for publication in *Nucl. Instr. Meth.*, this chapter is somewhat cursory, expanding a bit on a few issues not dealt with in the paper with the same detail.
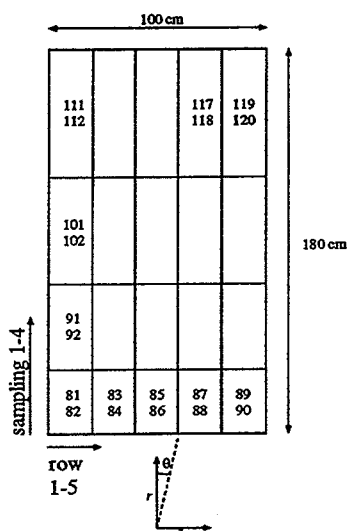

Figure 6.1: Cell layout and dimensions of a 1 m Tilecal prototype. Numbers refer to the PMT (channel) numbers of Module 3.

6.1 Description of the 1 m Prototypes

The prototype modules each correspond to a $2\pi/64$ slice in azimuth (ϕ), with a front face of ± 50 cm in z (horizontal direction, perpendicular to the test beam) and ± 10 cm in the ϕ direction. The prototype modules are 180 cm in depth, corresponding to 9.0 nuclear interaction lengths, λ, deeper than the final ATLAS design. The five modules are stacked, covering together a ϕ-angle of approximately 28°. A module has four radial (depth) segmentations: 1.5, 2.0, 2.5 and 3.0 λ (30, 40, 50 and 60 cm). In the z-direction the samplings are divided into five nearly equal cells each (12, 11, 11, 11 and 12 periods respectively). Towers are defined as cells with like z and ϕ. Fig. 6.1 is a sketch of the cell layout for one module.

Each cell is read out independently from the two sides, totalling 40 PMTs per module. The numbers in the figure correspond to channel numbers in Module 3. Four channels in Module 3 were not equipped with FERMI (117-120), and nine more were faulty or had bad calibrations (82, 83, 90-92, 109-112), leaving 27 channels with double read-out for this analysis.

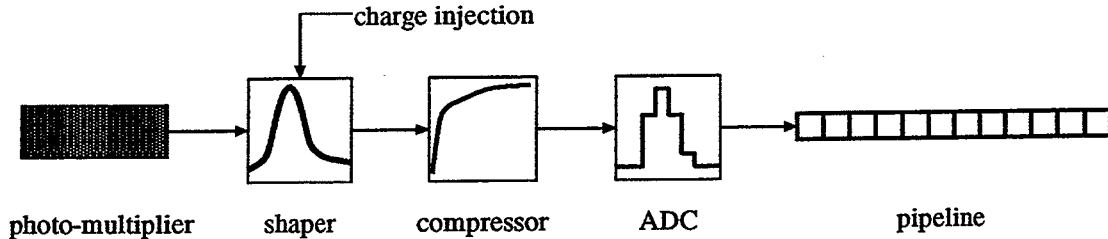# 6.2 The Fermi Analog Channel Prototype

Figure 6.2: Block scheme of FERMI read-out components. The digital pipeline has not been part of these tests.

The prototype of the FERMI system tested in July 1995 consisted of a compressor and a 10-bit sampling ADC, see Fig. 6.2.

The shaper takes input from either the photo-multiplier or the charge injection circuitry and delivers a 200 ns wide pulse (FWHM) in the 0–2 V range on the output. The compressor, schematically shown in Fig. 5.6, subsequently takes this signal and performs a non-linear compression, transforming the signal according to an approximately piecewise linear transfer function with four segments, producing again on the output a signal in the 0–2 V range.

The compressed signal is sampled at 40 MHz frequency by a custom designed 10 bit sampling ADC [26], which feeds a 256 sample FIFO. In this prototype the compressor and the FIFO sit on a two part VME board giving more flexibility

to swap parts during testing.

At the trigger, the ADC starts digitizing at the next clock cycle. The signal is delayed so that approximately twenty samples are taken before the peak. In total sixty consecutive ADC samples are stored to contain the pulse. The FIFO is then read out by the standard DAQ and data are stored on tape.
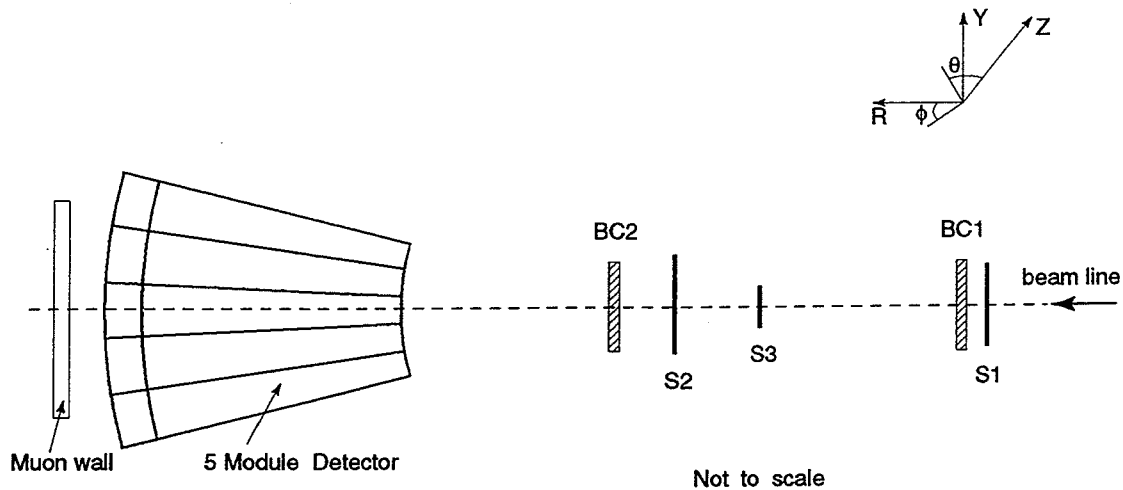

Figure 6.3: Test beam layout for the 1995 standalone test beam.

6.3   Beam Line

Measurements were performed in the H8 beam line of the SPS at CERN. The stack of five prototype modules was mounted on a scanning table which allowed precise movements in θ, ϕ and z. The beam line (Fig. 6.3) was instrumented with two beam chambers defining the impact point and three scintillators for triggering.

There were two scintillator walls, behind and to the right of the calorimeter, in the beam direction, tagging events with longitudinal and lateral leakage, assisting with muon identification. They have not been used in this work.

6.4   Precision Pulse Generator

The Precision Pulse Generator (PPG) used for the 1995 run was previously used in the UA2 experiment[27]. Three eight channel PPG-modules are fed a 100 V DC voltage. This voltage can be divided down using a resistor ladder, according to a logarithmic scale, with 14 steps. The PPG HV feeds a capacitor on each channel which on a remote command is shorted by an Hg relay. Each channel
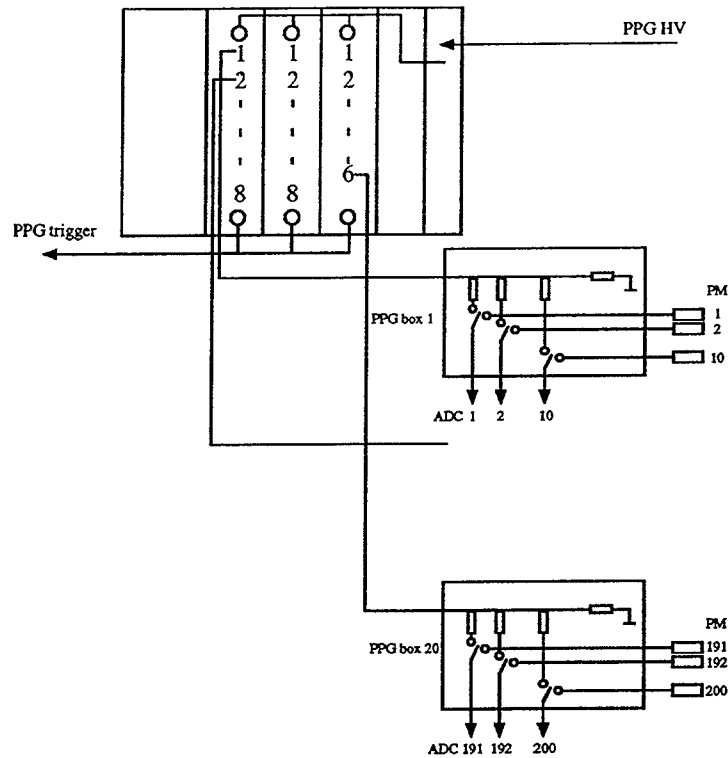
Figure 6.4: Layout of the PPG system.

is connected to a PPG box which in turn either distribute the signal from one PPG channel to ten ADC-inputs or connects ten PMTs to their respective ten ADC-channels (see Fig. 6.4).

6.5   Energy Estimates

In the data taken 1995 each event is a time frame of 60 ADC-samples. Since the height of the shaped pulse is supposed to correspond to the charge released in the PMT it would in principle be enough to estimate the top sample of the pulse, and deconvolute that with an inverse of the compression function, to correctly determine the energy. However, this estimate is quite sensitive to time jitter. The value of the top sample (indeed, any sample) will vary depending on the random phase between the FERMI clock and the trigger. This relationship is clearly illustrated in Fig. 6.5 for the peak sample for two different amplitudes. For large amplitudes, this effect is not so pronounced, since the large compression factor makes the peak rather flat. However, due to the larger amplification in this region, the effect on the resolution is larger. The spread due to time jitter is approximately 20 counts for low amplitude and 9 for high. In ATLAS the clock

of the ADCs will be synchronous with the colliding beams, hence the time jitter will not be an issue. For test beam purposes this effect is, however, present.
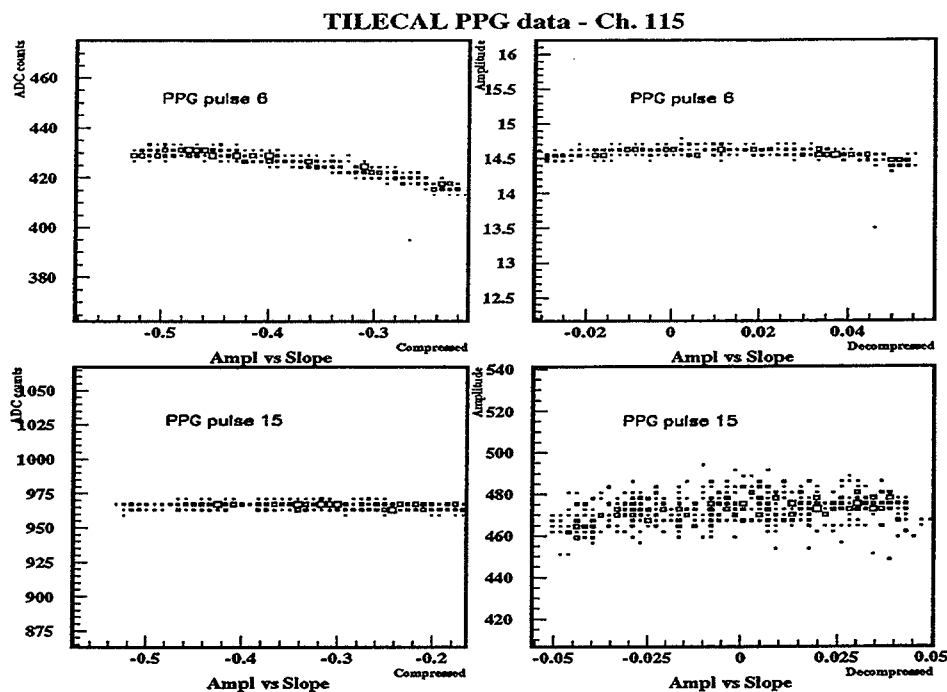

Figure 6.5: Peak amplitude versus slope (phase estimator) for compressed (left, in ADC counts) and decompressed (right, in pC) PPG pulses PPG6 (top) and PPG15 (bottom).

The rise and decay time of a PMT is significantly less than the characteristic time of the shaper. This means we can assume that the shaper gives the same response, modulo height, to all events. Likewise, the discharge time of the capacitor in the PPG system is short. This means that any sample, or a linear combination of samples, can be used as an energy estimate.

In a sum of several samples, a sample to the left of the peak will increase with increasing phase while one to the right will decrease. Hence, the contribution to the resolution due to time jitter will tend to cancel. On the other hand, the more samples that are added in, the more sensitive the energy estimate gets to electronic noise.

Given the pulse shape and a model for the noise it is possible to calculate coefficients in front of the samples to optimize the resolution of the estimate, getting what is called an optimal filter; this is detailed in [28, 29, 30, 31, 32, 33].

The pulse of the 1995 shaper was fairly wide compared to the sampling frequency and it turned out that using optimal filters as compared to filters with unity coefficients (straight adders) didn't improve the resolution significantly. In this analysis only straight adders have been used.

The next four sections will deal with lookup table construction and determination of the pulse shape.

6.6   Lookup Tables

In order to relate the 10-bit ADC digitization to the 16-bit dynamic range of the input data one has to know the inverse of the compression function of the compressor. This inverse function will be implemented in the form of a lookup table. The most straightforward approach would be to measure these in a quasi-static way in the laboratory, slowly varying the applied voltage on the input and recording the corresponding response on the output. However, this is not practical, and it would also not give a true picture of any effects due to the interplay between read out electronics and the PMTs. Instead, the PPG charge injection system is used to mimic PMT pulses with controlled amplitudes.

If we could choose the amplitudes of the charge injection system with adequate granularity and control the phase of the injected pulse with respect to the clock of the ADC it would be a fairly straightforward procedure to determine the amplitude and shape dependence of the compression function.

With the PPG system used in the 1995 run, however, only 14 amplitude settings were available and there was no way to fix or directly measure the relative timing between the pulse and the ADC clock. Below we describe more complex methods required to extract this information and how to use it to derive the lookup tables.

6.7   Determining the Pulse Shape

A priori, the shape of the pulse is only known with the granularity of the sampling interval (25 ns). To estimate it better we need an estimate of the phase between the ADC clock and the trigger and use that to rebin the events with finer granularity.

6.7.1   Using the Slope as a Phase Estimate

Using the fact that the pulse is a smooth function close to its peak we can estimate the phase by comparing two samples straddling the peak. We let our phase estimator be $S = (s(l) - s(r))/(s(p))$, where $s(l)$, $s(r)$ and $s(p)$ are the amplitudes at the samples $l = 19$, $r = 23$ and $p = 21$, respectively. The value of $p = 21$ as the peak sample is dictated by a delay fixed by hardware. This estimator
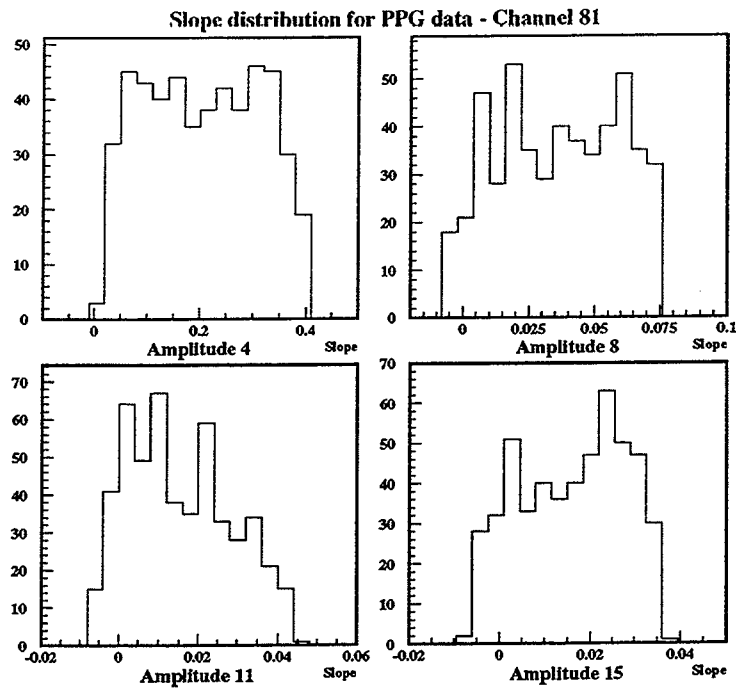
Slope distribution for PPG data - Channel 81

Figure 6.6: Distribution of the slope variable.

is not linear with the phase, but maintains a distribution like Fig. 6.6. Assuming the distribution of the phase to be flat, we can rebin the slope histograms with bins of unequal width, but equal number of entries, and thus linearize this phase estimate.

6.8 Three Parameter Fit

The different gains of the compressor could vary slightly due to spread in component values, mostly in the supporting circuits. The value of the cutoff voltage could also vary. To the first order these effects can be taken into account by taking a model lookup table and distort it slightly, by stretching and translating. For a few channels the complete lookup tables have been measured in the laboratory quasi-statically as mentioned above. These tables were then taken as model lookup tables.

In this method we only use the peak amplitude of the pulse shapes, estimated by a fit of a second degree polynomial to the peak region of the pulse shape, and the nominal PPG charge values for the corresponding pulses. The model lookup table is then stretched and translated so as to minimize the distance between the

lookup table and the PPG points.

6.9   Pulse Shape Comparison

In the second method, we use more of the information available. The additional assumption made here is that the shaper output scales linearly with the charge, so as to make the shape invariant. This assumption is only partially valid, though, as we will see further on.

The scaling factor is known a priori in the case of PPG calibration as the charge injected; we will label it E_n. In the procedure that we outline we assume a priori knowledge of the lookup table $V(k)$ for a limited range of ADC values at the low end. The choice of such initial lookup table is not critical; in the low region the lookup table should be linear. It has also been demonstrated that this "initial" $V(k)$·can be done away with and the lookup table be built using only measured PPG data and the values of the injected charge (which are, in principal, also unnecessary).

The pulse shapes reconstructed as above are denoted $s_n(i)$ where i indexes time in bins of 1 ns, and n enumerates the different PPG amplitudes. One such pulse is chosen as reference, small enough to reside entirely within the first linear slope, but large enough to stand clear of noise; this pulse is referred to as $s_{ref}(i)$.

In principle this pulse, and the highest pulse available, together define the lookup table. This fact will be used when looking at the pulse shape distortions (Sec. 6.9.1). However, we choose to build the lookup table in pieces, using each intermediate pulse height.

The ADC-axis is divided into intervals between peak values of successive PPG pulses, as indicated in Fig. 6.7. In each such interval we use the reference pulse and the pulse defining the upper end of the interval to make the lookup table.

The reference pulse is then normalized to the energy scale of the pulse under consideration. Because of the shape invariance, this should correspond to what the compressor sees on the input when it produces the compressed pulse s_n on the output:

$$V(s_n(i)) = \frac{E_n}{E_{ref}} V(s_{ref}(i)),$$

where $V(k)$ denotes the true (ideal) lookup table, and E_{ref} the (injected) charge of the reference pulse.

The pulse will cross each ADC-value k twice, once on the rising edge, and once falling back to baseline on the trailing edge. We average over these two values.

Because of the time slew effect present in the 1995 test beam setup (discussed further in Sec. 6.9.1) the invariance of the pulse shape for different amplitudes is only approximate. Parts of the pulse rising or falling at different speeds will be
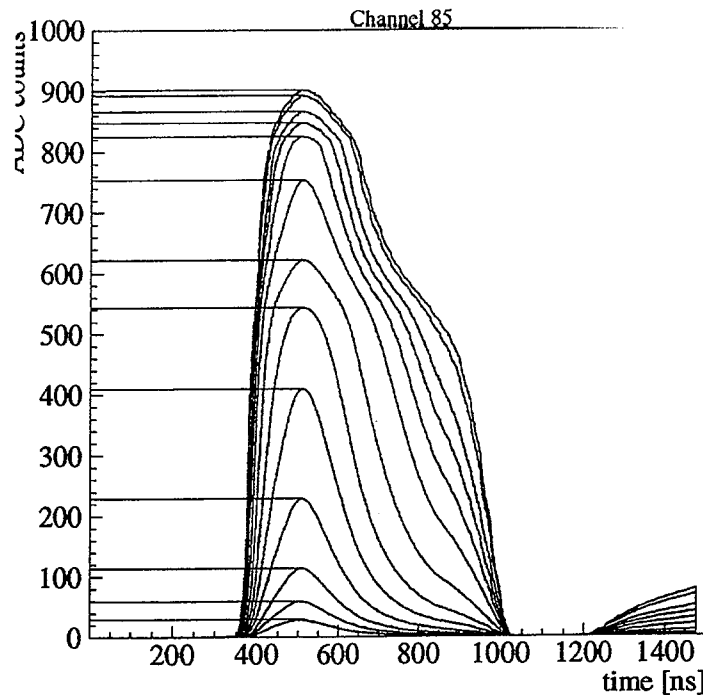
Figure 6.7: PPG pulse shapes, pulses 2 through 15. The intervals on the ADC-axis between successive peak values have been indicated with lines.

slightly differently compressed. The effect is to give different compression functions for the rising and falling edges of the pulse, due to the significantly different absolute magnitude of their derivatives. The effect of this will differ depending on which energy estimator is used, as different samples (relative to the peak) will be weighted in differently. This effect is taken into account by applying the lookup table and the energy estimator to the PPG pulses and subsequently multiplying the lookup table entries in each interval by a correction factor and finally smoothing the resulting curve by a weighted average.

The structure of this method is motivated by the intended design of the hardware LUT that would be used to decompress data for the level 1 trigger, in the case of a digital trigger summation.

6.9.1 Pulse Shape Distorsion

It was noted that there were some time slewing effects present in the shaper/compressor stage of the 1995 setup, thus voiding the hypothesis of shape invariance to some extent. The effect is visualized in Fig 6.8. In the plot to the left we have two reconstructed compressed pulse shapes, one in the linear region (ampli-
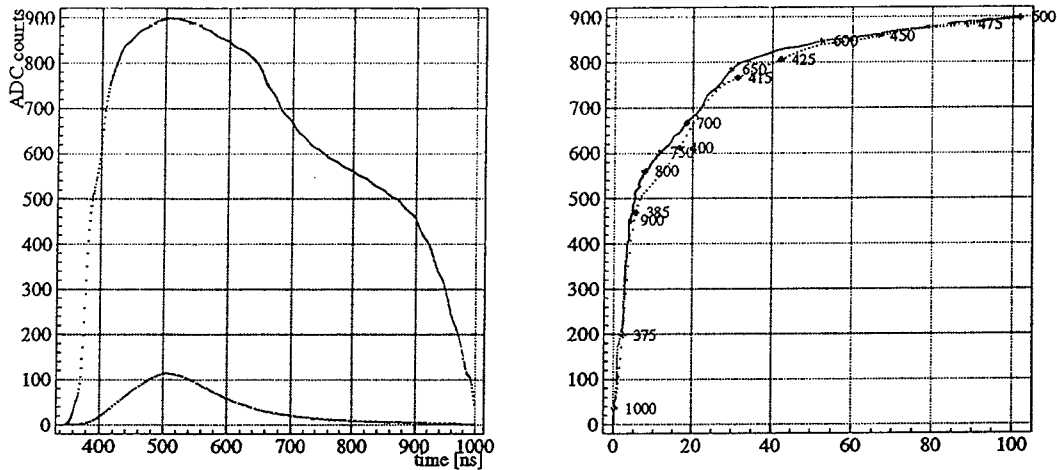
Figure 6.8: Left: PPG pulse shapes 15 and 5. Right: PPG pulse 15 vs pulse 5, $(q_{15}s_5(i), s_{15}(i))$. The numbers indicate the time (in ns).

tude 5, $s_5(i)$, our reference pulse), and one at the top end (amplitude 15, $s_{15}(i)$). The plot to the right is a parametric plot $(x, y) = (q_{15}s_5(i), s_{15}(i))$, where i runs from 0 to 1500 ns. For clarity, there are numbers marking the time. We scale the reference pulse by the charge of the large pulse, q_{15}. The pulses rise fairly fast, leaving the sparse lower trail. At 500 ns both curves peak, and start falling back towards baseline, although more slowly, leaving the denser upper trail. Hence, on the rising edge the large pulse exhibits a larger compression factor as compared to the small pulse, than it does on the falling edge. This means that the shape invariance is not exact.

The effect can be understood from the fact that in an op-amp there is a limit in the rate at which the output can change due to the compensation capacitance and small internal drive currents. This limiting rate is referred to as the slew rate. Hence, for large pulses, the output of the shaper/compressor stage cannot change fast enough to follow the rising edge. The falling edge has a much smaller derivative, so that the slew rate limitation does not set in.

In the two plots on the left in Fig. 6.9 the three PPG pulse shapes for amplitudes 15, 11 and 6 are plotted, together with the corresponding time derivatives. To the right there are three parametric plots of the same type as in Fig. 6.8 overlaid for amplitudes 15 vs. 5, 11 vs. 5 and 6 vs. 5. The reference pulse has, in each plot, been scaled with the injected charge of the large pulse, in order to relate the x-scales to each other. The first plot is the one running all the way to $(100, 900)$, and has the largest deviation on the rising edge; the second runs to approx. $(40, 820)$ and deviates slightly less. The third plot runs to $(5, 400)$, not leaving the first region of the compressor. The distortion of the rising, fast, edge is thus different for
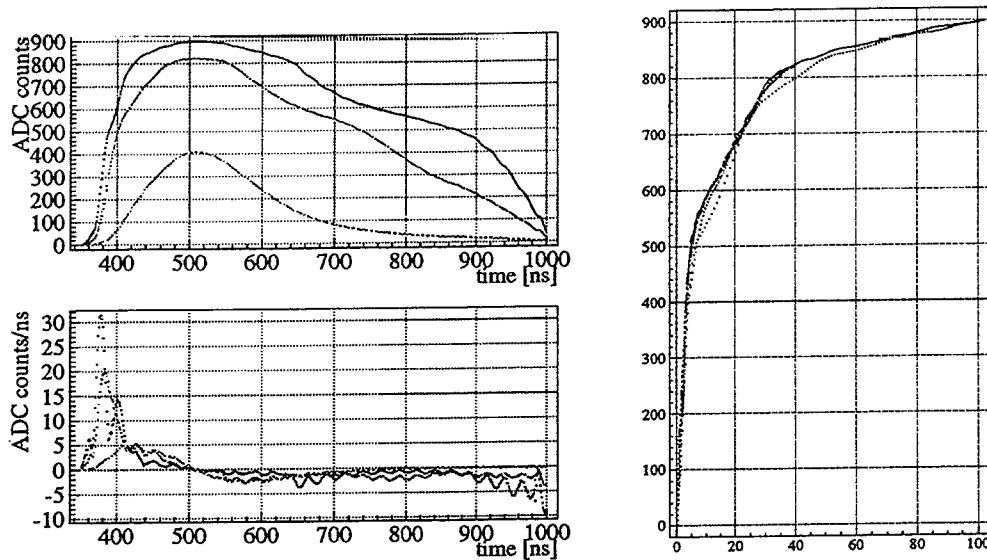
Figure 6.9: In the top left plot the pulse shapes of PPG pulses 15, 11 and 6 are shown. In lower left plot the corresponding time derivatives. Right: PPG pulse shapes amplitudes 15, 11 and 6 vs. the pulse shape of amplitude 5.

the three different amplitudes, while for the falling edge the same plot is always obtained. The interpretation of this is that the derivative of the falling edge is always below the slew rate, and hence this part of the pulse is never distorted. From the Fig. 6.9, we can estimate the slew rate to be to the order of 10 ADC counts/ns ($\approx$ 20 mV/ns).

For a sum of several samples, the different samples will thus experience different compression functions. This is taken into account by averaging the compression functions corresponding to the different samples and applying a linearization on the resulting lookup table, as described in Sec. 6.9 and in Sec. 4.2.2 of the enclosed paper.

6.10   Measures of Resolution

6.10.1   Intrinsic Resolution

Studies were performed to compare the intrinsic resolution of the two calibration methods. As a measure, the resolution of the charge injection data, when using the energy estimates mentioned above, is used. We also look at the deviations

from linearity of the reconstructed data. We study these quantities for different estimates as a function of adder length, and as a function of pulse amplitude. Naturally we expect good resolution and linearity, since these are the data from which the calibrations were made. Still, it provides an important crosscheck.

The important conclusions that come out of this study is that:

- The optimal adder length is about 11. For shorter adders, time jitters tend to dominate, while for longer adders noise starts to mount.

- The intrinsic resolution of the two calibration methods, at any given amplitude, is equivalent.

- The pulse shape comparison method gives a much better linearity than the three parameter fit. This is also expected, since each gain and each cutoff can vary very much independently and the dependance of the stretching parameters tend to be strongest on the points belonging to the first segment. The pulse shape comparison, on the other hand contains explicit linearizing.

6.11   Event Sample Selection

run	# events	type	θ [°]	z [cm]
33484	15205	300 GeV π^-	+10	−6
33485	15143	300 GeV π^-	+10	−8
33486	15172	300 GeV π^-	+20	−18
33487	15150	300 GeV π^-	+20	−20
33489	≈15000	300 GeV π^-	+30	−36
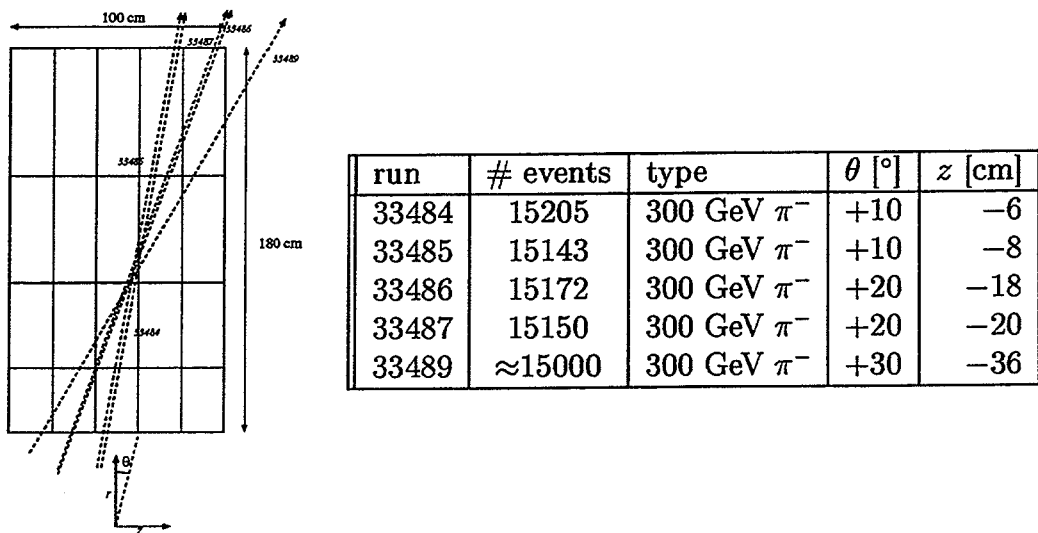
Figure 6.10: Impact point and directions of the beam of the runs considered in this analysis.

As mentioned in the introduction, the highest energy pion runs were selected for this analysis, as they have the smallest contribution from intrinsic and sampling fluctuations.

We use five runs of 300 GeV π^- with different angle and point of incidence with about 15000 triggers each (see Fig. 6.10). We note that these runs were

taken at a positive angle of incidence, meaning that the showers point into the four channels of Module 3 (117-119) that were not equipped with FERMI. In all cases the fraction of the total energy deposited in FERMI equipped channels varies between 75 and 90%.
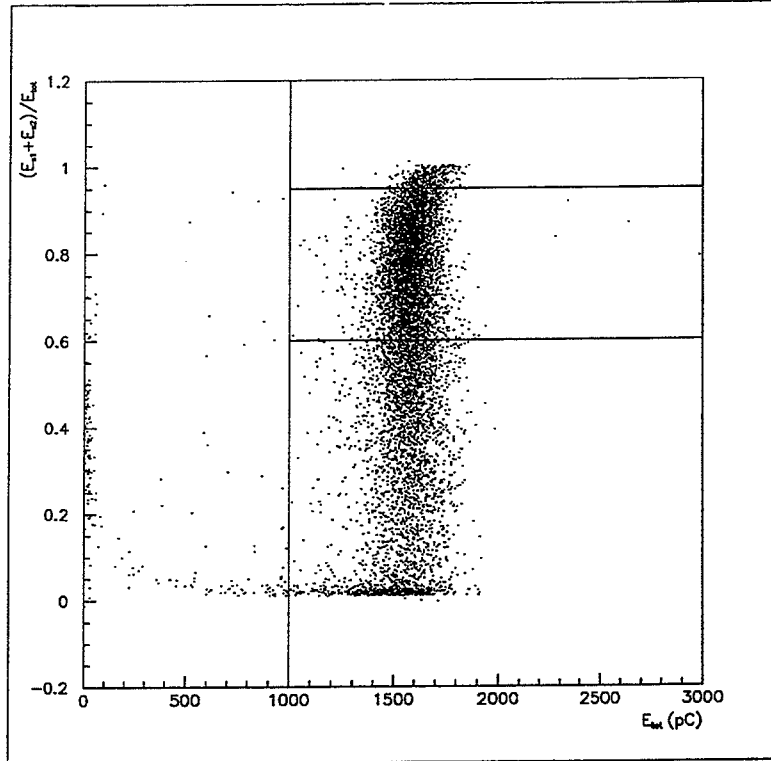

Figure 6.11: Fraction of energy deposited in sampling 1 and 2 vs. total energy with energy cuts indicated: $0.60 < (E_{\text{sampling1}} + E_{\text{sampling2}})/E_{\text{tot}} < 0.95$ and $E_{\text{tot}} > 1000$ The energy scale is approx. 0.18 GeV/unit (the figure illustrates run 33484).

The electron and muon contaminations of the beams are removed by demanding that between 60% and 95% of the energy is deposited in the first two sampling depths of the calorimeter. We also cut events that deposit less than approximately 180 GeV in the calorimeter (Fig. 6.11).

6.12 Resolution with Fermi and the Standard Electronics

The most straightforward method of comparing the two electronics would be to compare the reconstructed energy in the channels that were equipped with both

types of electronics. Due to the leakage into channels not equipped with FERMI the fluctuations of this quantity is quite large.

In order to compare quantities with less intrinsic spread, the energy released in the channels not equipped with FERMI was added to the energy of FERMI channels (i.e. 173 standard channels + 27 FERMI), and this quantity was compared to to the energy of 200 standard channels.

The total resolution can, in both cases, be written as a quadratic sum of one energy dependent term and several constant terms. The energy dependent term is the intrinsic spread in the measurements, depending only on the calorimeter, and the constant terms are contributions from leakage, from the electronics miscalibration, and, when considering the sum of 173 standard and 27 FERMI channels, from misintercalibration. Noise contribution is unimportant at the energy considered and is not included.

$$R_S = \left.\frac{\sigma}{E}\right|_S = \frac{a}{\sqrt{E}} \oplus C_{\text{leakage}} \oplus C_{S173} \oplus C_{S27},$$

$$R_F = \left.\frac{\sigma}{E}\right|_F = \frac{a}{\sqrt{E}} \oplus C_{\text{leakage}} \oplus C_{S173} \oplus C_{F27} \oplus C_{\text{misintercalib.}},$$

where the subscript S denotes standard read-out and F denotes FERMI.

When comparing only 27 channels the C_{S173} term does not contribute while lateral leakage in the ϕ direction makes C_{leakage} large; this term is, however, in common between the two different read-out electronics. When summing 200 channels the C_{S173} term gives a sizeable contribution while C_{leakage} is comparably smaller.

The quality of the electronics and our calibration method is measured with the quadratic difference, $\delta = \pm\sqrt{\left|\left(\left.\frac{\sigma}{E}\right|_F\right)^2 - \left(\left.\frac{\sigma}{E}\right|_S\right)^2\right|}$, between the resolutions, where negative sign of δ indicates that the standard term under the square root is larger than the FERMI term. This gives an estimate of the FERMI electronics contribution to the resolution.

The error in δ is a measure of the precision of our comparison. In calculating this error, it has to be considered that the read-out of the two electronics for each individual event is highly correlated.

6.13 Measured Resolutions

Table 6.1 and Tab. 6.2, for 200 channels, and Tab. 6.3 and Tab. 6.4 if we use only the 27 channels summarize the results. We see that the three parameter fit ("stretching") is slightly worse than the standard read-out. Most likely this is due to the limited linearity in the lookup table. The method based on linearized pulse shape comparison, on the other hand, performs significantly better than the standard electronics, at least for adequate filter lengths. This is not surprising, as this method provides higher control over linearity.

run		33484	33485	33486	33487	33489
trad		5.16 ± 0.06	5.73 ± 0.08	4.36 ± 0.05	4.36 ± 0.05	4.67 ± 0.06
3PF	5	5.55 ± 0.07	6.13 ± 0.09	4.84 ± 0.06	4.75 ± 0.06	4.73 ± 0.06
3PF	11	5.39 ± 0.07	5.96 ± 0.09	4.61 ± 0.05	4.58 ± 0.05	4.69 ± 0.05
3PF	I	5.35 ± 0.07	5.87 ± 0.08	4.51 ± 0.05	4.49 ± 0.05	4.57 ± 0.05
PSC	5	5.14 ± 0.06	5.81 ± 0.08	4.41 ± 0.05	4.42 ± 0.05	4.71 ± 0.05
PSC	11	5.04 ± 0.06	5.59 ± 0.07	4.31 ± 0.05	4.32 ± 0.05	4.61 ± 0.05
PSC	I	5.03 ± 0.06	5.60 ± 0.07	4.20 ± 0.05	4.25 ± 0.05	4.48 ± 0.05

Table 6.1: Resolutions in percent for traditional electronics (trad.), three parameter fit (3PF) and pulse shape comparison (PSC) for full integrator (I), 5-adder and 11-adder for five runs (cf. Fig. 6.10), using 200 channels.

run		33484	33485	33486	33487	33489
3PF	5	2.03 ± 0.06	2.19 ± 0.07	2.10 ± 0.05	1.89 ± 0.06	0.77 ± 0.07
3PF	11	1.56 ± 0.05	1.67 ± 0.07	1.48 ± 0.05	1.42 ± 0.07	0.48 ± 0.10
3PF	I	1.42 ± 0.06	1.28 ± 0.11	1.17 ± 0.07	1.10 ± 0.10	-0.95 ± 0.08
PSC	5	-0.44 ± 0.15	0.98 ± 0.10	0.63 ± 0.10	0.71 ± 0.14	0.65 ± 0.07
PSC	11	-1.10 ± 0.05	-1.22 ± 0.07	-0.68 ± 0.08	-0.56 ± 0.17	-0.73 ± 0.06
PSC	I	-1.17 ± 0.04	-1.21 ± 0.09	-1.18 ± 0.07	-0.98 ± 0.11	-1.32 ± 0.05

Table 6.2: Quality measures, δ, for three parameter fit (3PF) and pulse shape comparison (PSC) for full integrator (I), 5-adder and 11-adder for five runs (cf. Fig. 6.10), using 200 channels.

run		33484	33485	33486	33487	33489
trad		8.39 ± 0.11	8.55 ± 0.12	12.17 ± 0.13	13.14 ± 0.15	14.79 ± 0.17
3PF	5	8.74 ± 0.12	8.95 ± 0.12	13.03 ± 0.15	13.52 ± 0.16	14.94 ± 0.18
3PF	11	8.63 ± 0.12	8.75 ± 0.12	12.76 ± 0.14	13.40 ± 0.16	14.73 ± 0.17
3PF	I	8.57 ± 0.12	8.80 ± 0.13	12.73 ± 0.15	13.28 ± 0.16	14.61 ± 0.16
PSC	5	8.27 ± 0.10	8.52 ± 0.11	12.27 ± 0.13	12.91 ± 0.14	14.55 ± 0.15
PSC	11	8.15 ± 0.10	8.49 ± 0.11	12.08 ± 0.13	12.88 ± 0.14	14.43 ± 0.16
PSC	I	8.17 ± 0.11	8.38 ± 0.11	11.95 ± 0.13	12.75 ± 0.14	14.38 ± 0.15

Table 6.3: Resolutions in percent for traditional electronics (trad.), three parameter fit (3PF) and pulse shape comparison (PSC) for full integrator (I), 5-adder and 11-adder for five runs (cf. Fig. 6.10), using 27 channels.

run		33484	33485	33486	33487	33489
3PF	5	2.46 ± 0.09	2.64 ± 0.09	4.66 ± 0.09	3.15 ± 0.15	2.11 ± 0.13
3PF	11	2.04 ± 0.08	1.87 ± 0.10	3.86 ± 0.08	2.61 ± 0.17	-1.25 ± 0.17
3PF	I	1.77 ± 0.08	2.09 ± 0.11	3.73 ± 0.10	1.90 ± 0.26	-2.26 ± 0.14
PSC	5	-1.37 ± 0.09	-0.77 ± 0.21	1.61 ± 0.15	-2.45 ± 0.18	-2.61 ± 0.08
PSC	11	-1.96 ± 0.05	-1.00 ± 0.13	-1.48 ± 0.14	-2.64 ± 0.16	-3.24 ± 0.06
PSC	I	-1.90 ± 0.05	-1.73 ± 0.11	-2.28 ± 0.13	-3.19 ± 0.16	-3.43 ± 0.09

Table 6.4: Quality measures, δ, for three parameter fit (3PF) and pulse shape comparison (PSC) for full integrator (I), 5-adder and 11-adder for five runs (cf. Fig. 6.10), using 27 channels.

Looking at Table 6.1 the effect on the resolution from leakage in run 33489 can be seen. In run 33484, and more clearly 33485, worse resolution due to variations of the sampling fraction depending on angle of incidence is seen. In Table 6.3 the pattern is different, here runs 33486, 33487 and 33489 have much worse resolution. This is due to the fact that the shower in these cases mostly illuminate channels that were not equipped with FERMI.

With some approximation, the performance of FERMI can be summarized in a quadratic reduction of 1% of the constant term in the resolution.

6.14   Conclusions

A module of the ATLAS Tilecal prototype equipped with a preliminary version of the FERMI read-out system including a compressor and a sampling ADC has been successfully tested.

We have been using charge injection data to reconstruct the inverse of the compression function, individually for each channel, the lookup tables, in a way that minimizes amplitude dependent distorsions and non-linearity.

These techniques, together with the use of linear filters to process the sampled data, allow to improve the energy resolution relative to the one obtained with standard integrating ADCs.

Acknowledgements

Bibliography

[1] S. L. Glashow, Nucl. Phys. **22**, 579 (1961).

[2] A. Salam, Weak and electromagnetic interactions, in *Nobel Symposium 8: "Elementary Particle Physics Theory"*, edited by N. Svartholm, pages 367–377, Almqvist & Wiksell, Stockholm, 1968, held at Aspenäsgården, Lerum.

[3] S. Weinberg, Phys. Rev. Letters **19**, 1264 (1967).

[4] P. S. Drell, Experimental aspects of the Standard Model: A short course for theorists, hep-ex/9701001.

[5] The LEP Collaborations ALEPH, DELPHI, L3, OPAL, the LEP Electroweak Working Group and the SLD Heavy Flavour Group, A combination of preliminary electroweak measurements and constraints on the Standard Model, CERN-PPE/96-183.

[6] W. de Boer, A. Dabelstein, W. Hollik, W. Mösle, and U. Schwikerath, Global fits of the SM and MSSM to electroweak precision data, in *Proc. ICHEP96 Conference in Warsaw*, 1996.

[7] W. Hollik, Review of the electroweak theory, 1996, Talk given at ICHEP96 Conference in Warsaw.

[8] J.-F. Grivaz, New particle searches, Talk given at International Europhysics Conference on High Energy Physics, Brussels, Belgium 1995, LAL 95-83.

[9] J. Martin, Higgs particle searches at LEP, 1996, Talk given at ICHEP96 Conference in Warsaw.

[10] E. Accomando et al., Higgs physics, in *Physics at LEP2 Vol 1*, edited by G. Altarelli, T. Sjöstrand, and F. Zwirner, pages 351–462, 1996, CERN 96-01.

[11] G. F. Giudice, Beyond the Standard Model, hep-ph/9605390.

[12] C. Csáki, The Minimal Supersymmetric Standard Model (MSSM), MIT-CTP-2542, hep-ph/9606414.

[13] S. Dawson, SUSY and such, Lectures given at NATO Advanced Study Institute on Techniques and Concepts of High Energy Physics, July 11-22, 1996, St. Croix, Virgin Islands.

[14] The LHC Study Group, The Large Hadron Collider – conceptua design report, 1995, CERN/AC/95-05(LHC).

[15] K. Potter, The Large Hadron Collider (LHC) project of CERN, LHC Project Report 36, 1996, Talk given at ICHEP96 in Warsaw.

[16] R. Wigmans, Nucl. Instr. and Meth. **A265**, 273 (1988).

[17] T. Gabriel, D. Groom, P. Job, N. Mokhov, and G. Stevenson, Nucl. Instr. and Meth. **A338**, 336 (1994).

[18] ATLAS — letter of intent for a general-purpose pp experiment at the Large Hadron Collider at CERN, 1992.

[19] ATLAS — technical proposal for a general-purpose pp experiment at the Large Hadron Collider at CERN, 1993.

[20] ATLAS Tile Collaboration, ATLAS tile calorimeter technical design report, CERN/LHCC/96-42.

[21] R. Wigmans, Nucl. Instr. and Meth. **A259**, 289 (1987).

[22] K. Anderson et al., A low noise, high rate shaper for the tilecal detector, Talk at the First Workshop on Electronics for LHC Experiments, Lisbon, September 1995.

[23] F. Ariztizabal et al., Nucl. Instr. and Meth. **A357** (1994).

[24] E. Berger et al., Construction and performance of an iron-scintillator hadron calorimeter with longitudinal tile configuration, CERN/LHCC/95-44, 1995.

[25] Z. Ajaltouni et al. (ATLAS Collaboration, Calorimetry and Data Acquisition), Results from a combined test of an electromagnetic liquid argon calorimeter with a hadronic scintillating tile calorimeter, CERN-PPE/96-178, accepted for publication in *Nucl. Instr. Meth.*

[26] C. Svensson and J. Yuan, IEEE Journal on Solid State Circuits and Systems **29**, 866 (1994).

[27] A. Beer et al., Nucl. Instr. and Meth. **A224** (1984).

[28] P. W. Cattaneo, Nucl. Instr. and Meth. **A373**, 93 (1996).

[29] S. J. Inkinen, FIROSMIN 3.1 users guide, FERMI Note # 24.

[30] S. J. Inkinen et al., Nonlinear filters for pulse amplitude extraction in FERMI, in *Proc. IEEE Nuclear Science Symposium*, pages 687–691, 1994.

[31] S. J. Inkinen and J. Niittylahti, IEEE Transactions on Circuit and Systems-II: Analog and Digital Signal Processing **42**, 663 (1995).

[32] H. Alexanian et al., Nucl. Instr. and Meth. **A357**, 318 (1995).

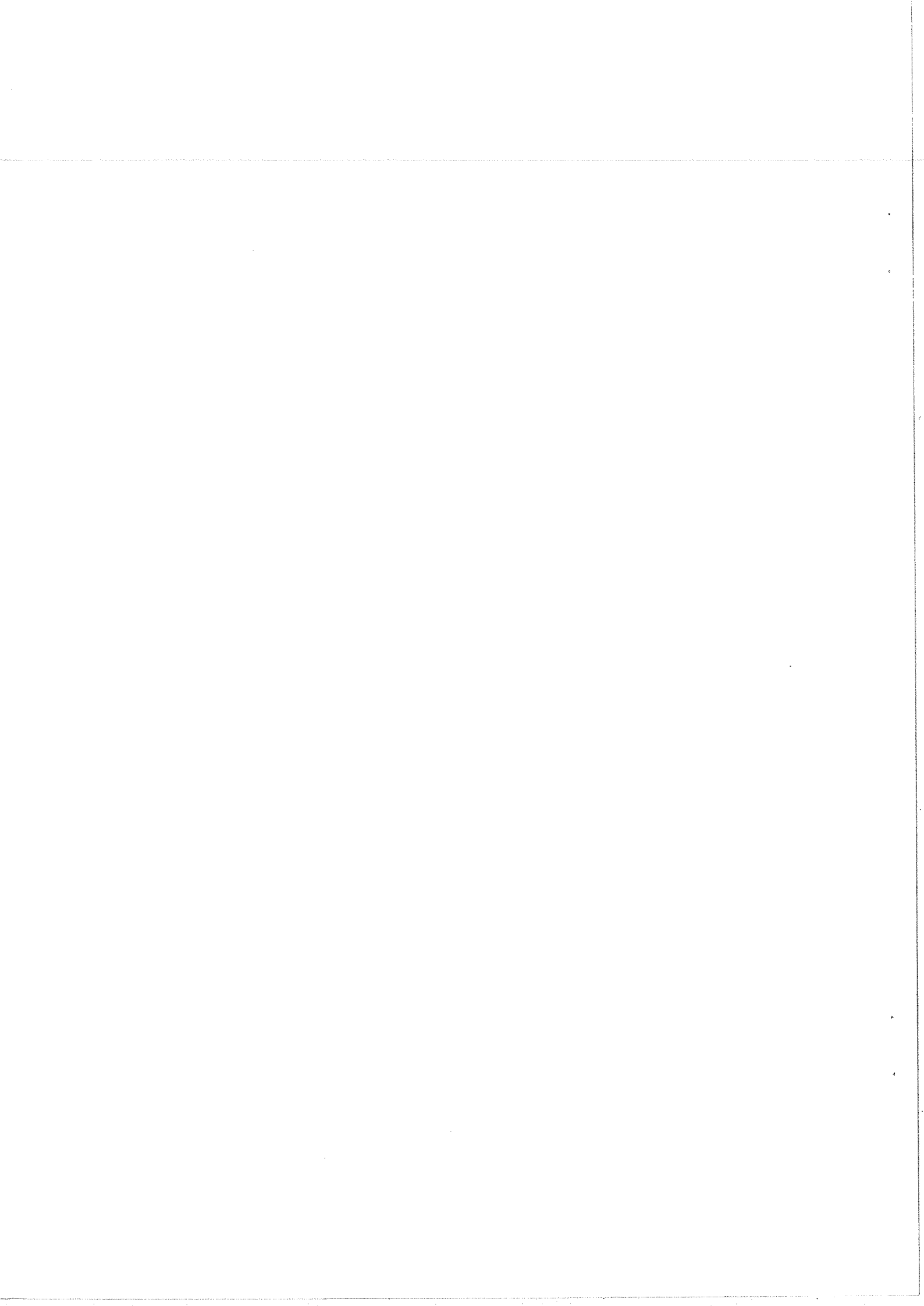[33] N. Launay, C. de la Taille, and L. Fayard, Noise improvement with multiple samples, ATLAS Note/CALO # 24.

List of Tables

List of Figures

Evaluation of Fermi Read-out of the Atlas Tilecal Prototype

J. A. Perlas

IFAE, Barcelona, Spain

K. Anderson, H. Evans, J. Pilcher, H. Sanders, F. Tang

University of Chicago, Chicago, USA

R. Benetta, M. Cobal, I. Efthymiopoulos, M. Hansen, A. Rios

CERN, Geneva, Switzerland

P. W. Cattaneo[1], G. Polesello

Dipartimento di Fisica Nucleare e Teorica dell'Università, Sezione INFN,

Pavia, Italy

S. Agnvall, S. Berglund, Ch. Bohm, A. Fristedt, S. Hellman,
S.-O. Holmgren, K. Jon-And, B. Selldén, S. Tardell,
N. Yamdagni

Department of Physics, Stockholm University, Sweden

Abstract

Prototypes of the FERMI system have been used to read out a prototype of the ATLAS hadron calorimeter in a beam test at the CERN SPS. The FERMI read-out system, using a compressor and a sampling ADC, is compared to a standard charge integrating read-out by measuring the energy resolution of the calorimeter separately with the two systems on the same events.

Signal processing techniques have been designed to optimize the treatment of FERMI data. The resulting energy resolution is better than the one obtained with the standard read-out.

Keywords: Calorimetry; Signal processing; Read-out electronics

---

[1] Corresponding author. Via A. Bassi 6, I-27100 Pavia, Italy Tel.: +39 382 75 78, fax: +39 382 42 32 41, e-mail cattaneo@pv.infn.it
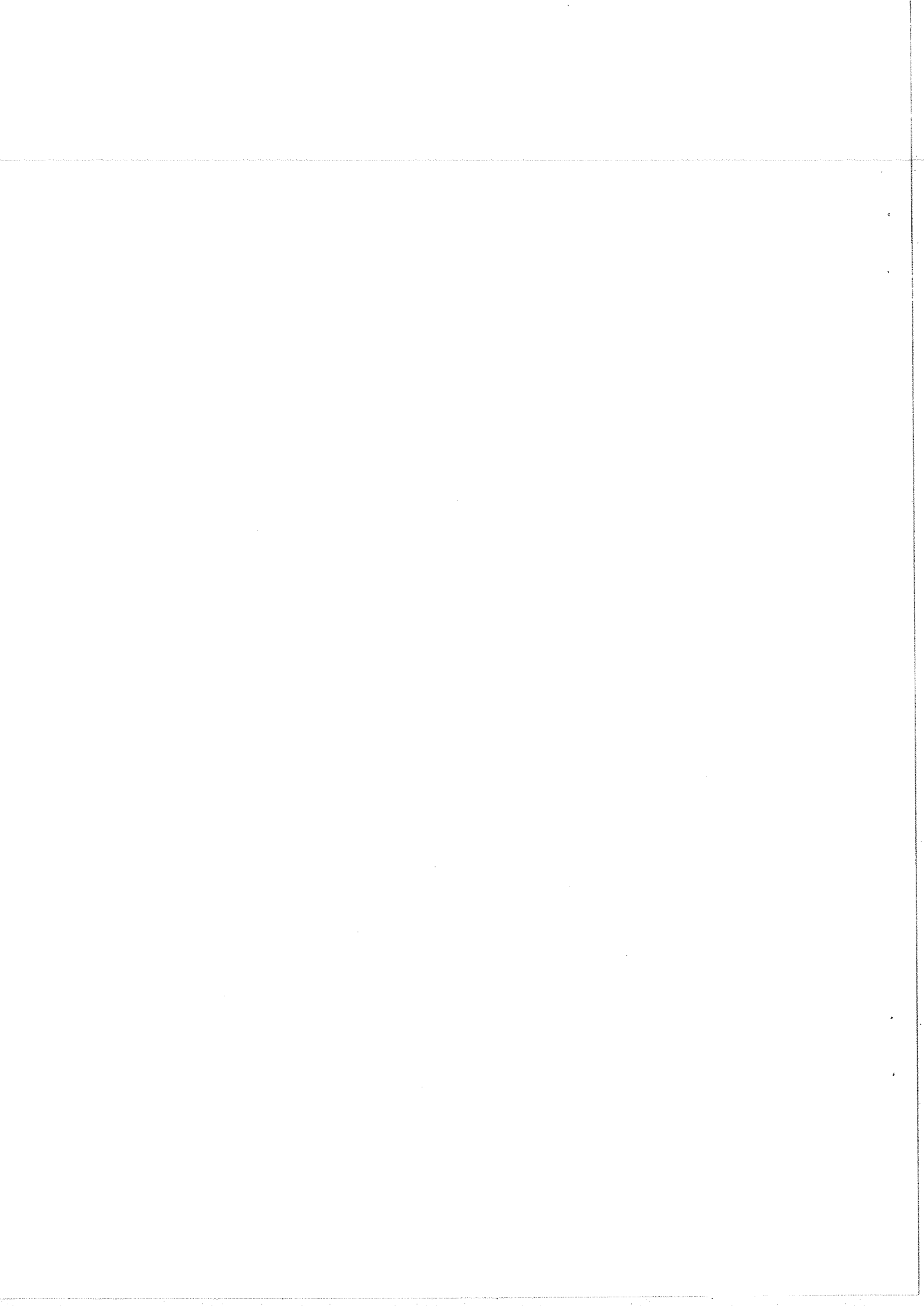
1. Introduction

This paper summarizes the evaluation of the FERMI system prototypes used to read-out a prototype of the ATLAS hadronic barrel calorimeter, Tilecal, during the July 1995 beam tests at the CERN SPS.

Tilecal is an iron-scintillator sampling hadron calorimeter with the distinctive feature that the scintillating tiles are oriented parallel to the impinging particles.

The major goals of the calorimeter are to identify jets and to measure their energy and direction, to measure the total missing energy and to enhance the particle identification of the electromagnetic calorimeter by measuring leakage and isolation. Additionally, the hadronic calorimeter should absorb all particles before they reach the muon chamber system, and provide low p_T muon identification.

To meet these goals the design aims at a resolution of $50\%/\sqrt{E} \oplus 3\%$, a linearity of 1–2% up to a few TeV and a granularity in pseudo-rapidity and azimuthal angle of $\Delta\eta \times \Delta\phi = 0.1 \times 0.1$.

The need to resolve low energy muons sets the lower end of the dynamic range, 15 ADC counts are required for a muon depositing 0.5 GeV per read-out cell. From simulations, the maximum expected energy per cell in Tilecal is about 2 TeV, at a rate of a few events per year. This gives a required dynamic range of approximately 2^{16}.

The overall performance of the Tilecal prototype is reported in [1, 2, 3, 4, 5] and the current status of the project is described in detail in the ATLAS Tile Calorimeter Technical Design Report [6].

The FERMI prototypes consist of an analog compressor and a 10 bits sampling ADC operating at 40 MHz on a custom VME board.

2. The Fermi Analog Channel

The FERMI project was started in 1990 with the aim to design a read-out system for calorimetry at high luminosity hadron machines, based on the concept of fast digitization of the analog signal followed by digital signal processing. For applications at the LHC, the basic requirement is to match the dynamic range implied by the physics (15–16 bits) with the ADC range (10–12 bits) technically feasible at the required digitization rate (40 MHz). This is achieved by a dynamic non-linear compressor. The project is described in detail in [7, 8] and references therein. A schematic layout of the system is shown in Fig. 1.

The shaper takes input from either the photo-multiplier or the charge injection circuitry and delivers a 200 ns wide pulse (FWHM) in the 0–2 V range on the output. The compressor, schematically shown in Fig. 2, subsequently takes this signal and performs a non-linear transformation, compressing the signal according to an approximately piecewise linear transfer function, producing on the output a signal in the 0–2 V range.
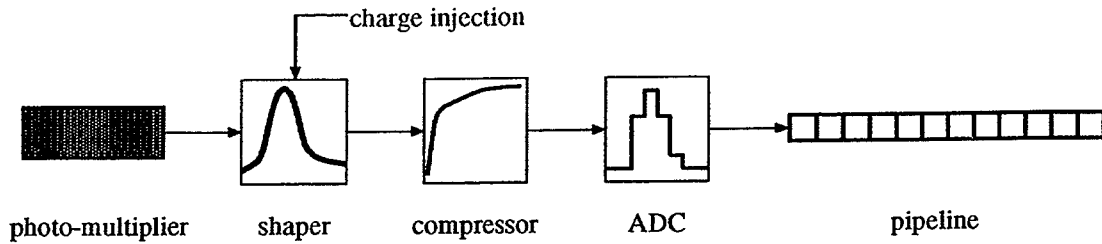
Figure 1: Block scheme of the read-out system. The digital pipeline has not been part of these tests.
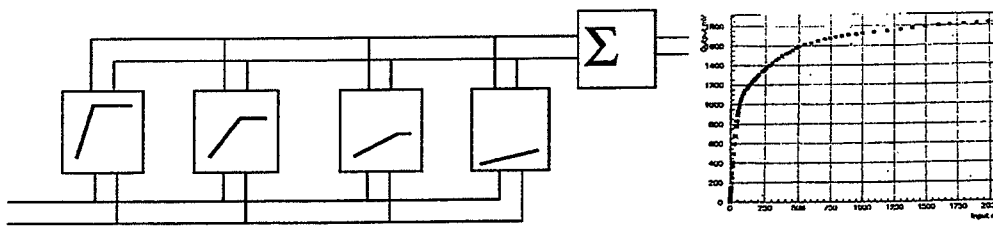

Figure 2: Concept of the compressor. This circuitry forms a sum of the outputs from four linear amplifiers with gains approximately 18.5, 1.3, 0.14 and 0.09 and upper cutoffs on the input voltage of 60, 470 and 1200 mV respectively. The fourth amplifier spans the full 2000 mV input range of the compressor. To the right, a typical transfer function as measured in the laboratory.

The compressed signal is sampled at 40 MHz frequency by a custom designed 10 bit sampling ADC [9], which feeds a 256 sample FIFO. The trigger starts the digitization at the next ADC clock cycle. The timing of the trigger is such that approximately twenty samples are taken before the peak. In total sixty consecutive ADC samples are taken to contain the pulse. The FIFO is then read out by the standard DAQ and data are stored on tape.

In Fig. 3 four single charge injection events of different amplitudes are shown. The regions of different gain are clearly shown on the two largest pulses, while the smallest is uncompressed, being totally within the first linear region of the compressor.

The compressed signals have to be relinearized before reconstruction of the calorimeter showers. This is conveniently done by mean of a lookup table for each channel. One of the main goals of this study is to devise and evaluate algorithms for the construction of these lookup tables from charge injection data. The design of the FERMI system foresees implementation of the lookup tables in hardware, thus allowing an online linearization and correction of the data.
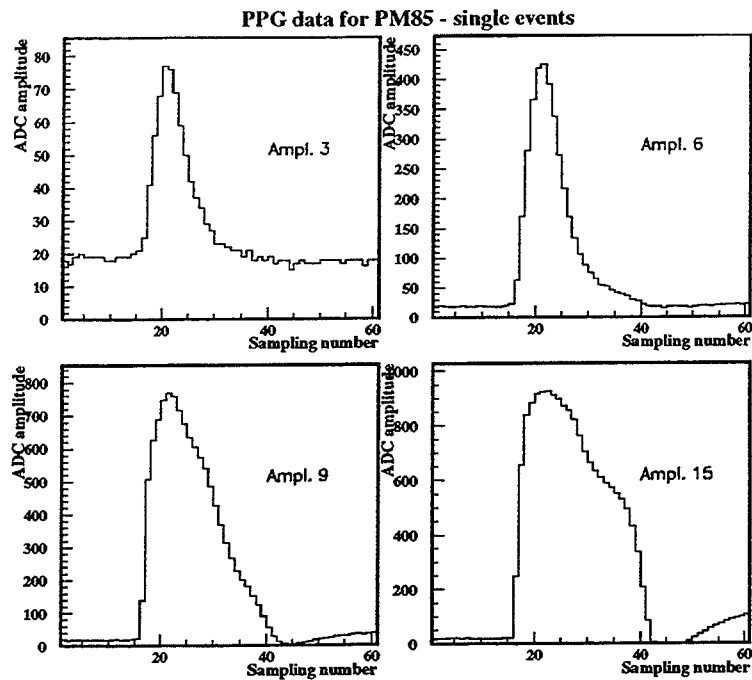
2

Figure 3: Example of four single charge injection events. Amplitude 3 is in the first linear region; amplitude 6 peaks at the first "knee", 9 at the second and 15 in the third region. Note the different scales.

3. Testing Fermi in a Test Beam with Tilecal

A small number of prototypes of the FERMI analog channels were tested in 1994 in test beams with both hadronic and electromagnetic barrel calorimeter prototypes [10, 11, 12].
In July 1995 a stack of five prototype modules of the ATLAS Tilecal Calorimeter was tested in beam at the CERN SPS.

3.1 Description of the 1 m Tilecal Prototype

Each prototype module (see Fig. 4) corresponds to a $2\pi/64$ slice in azimuth (ϕ), with a front face of ± 50 cm in z (horizontal direction, perpendicular to the beam) and ± 10 cm in the ϕ direction. In the radial direction (along the beam) the modules measure 180 cm, corresponding to 9 nuclear interaction lengths, λ. The five modules were stacked, covering together a ϕ-angle of approx. 28°. Each module has four radial (depth) segmentations corresponding to 1.5, 2.0, 2.5 and 3.0 λ (30, 40, 50 and 60 cm). In the z-direction each sampling is divided into five
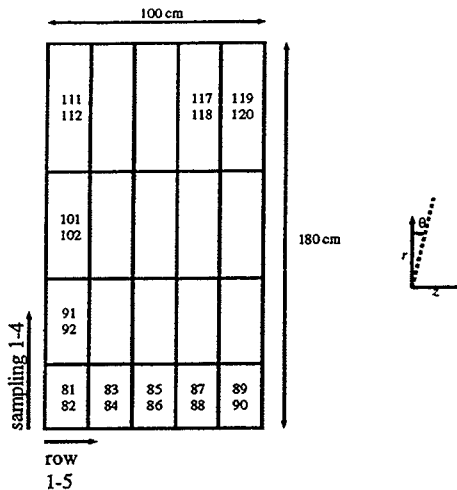
Figure 4: Cell layout and dimensions of a 1 m Tilecal prototype module. Numbers refer to the PMT (channel) numbers of the central module.

cells. Towers are defined as cells with the same z and ϕ. Fig. 4 is a sketch of the cell layout for one module.

Each cell is read-out independently from both sides, giving a total of 40 read-out channels per module. The central module in the stack was equipped with active splitters and double sets of read-out electronics, one based on standard integrating 12-bit ADCs, and one based on the FERMI concept. The numbers in Fig. 4 correspond to channel numbers in the central module. Four channels (117-120) were not equipped with FERMI, furthermore nine channels (82, 83, 90–92, 109–112) were faulty or not well calibrated, leaving 27 FERMI channels for this analysis.

3.2 Beam Line

Measurements were performed in the H8 beam line of the SPS at CERN. The stack of five prototype modules was mounted on a scanning table which allowed precise movements in θ, ϕ and z. The beam line (Fig. 6) was instrumented with two beam chambers defining the impact point and three scintillators for triggering.

The muon walls, placed behind the calorimeter and to the right in the beam direction, were not used in this analysis.

The runs considered for the analysis are described in Table 1 and in Fig. 7.

4
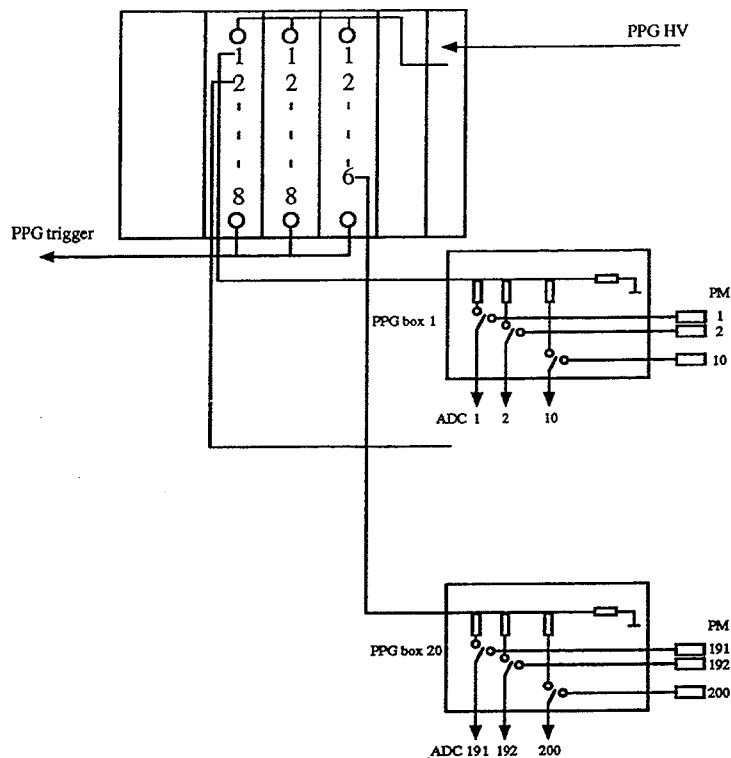
Figure 5: Layout of the PPG system.

3.3 Precision Pulse Generator

The Precision Pulse Generator (PPG) used for the 1995 run was designed for the calorimeter of the UA2 experiment [13]. Three eight-channel PPG-modules are fed a 100 V DC voltage. This voltage can be subdivided in 14 steps, using a resistor ladder, according to a logarithmic scale. The PPG HV feeds a capacitor on each channel which, on a remote command, is shorted by an Hg relay. Each channel is connected to a PPG box which in turn either connects ten PMTs to their respective ADC-channels or distribute the signal from one PPG channel to ten ADC-inputs (see Fig. 5).

4. Techniques for Fermi Calibration

In the 1994 beam tests the number of calorimeter channels equipped with FERMI was not large enough to exploit the energy resolution of the calorimeter as a tool to measure the performance of the FERMI electronics. Therefore other techniques were developed to infer the behaviour of FERMI. Several of these techniques provide valuable information on the detailed features of single channels and have been refined in the subsequent analysis [14, 15].

Figure 6: Test beam layout for the 1995 standalone test beam.

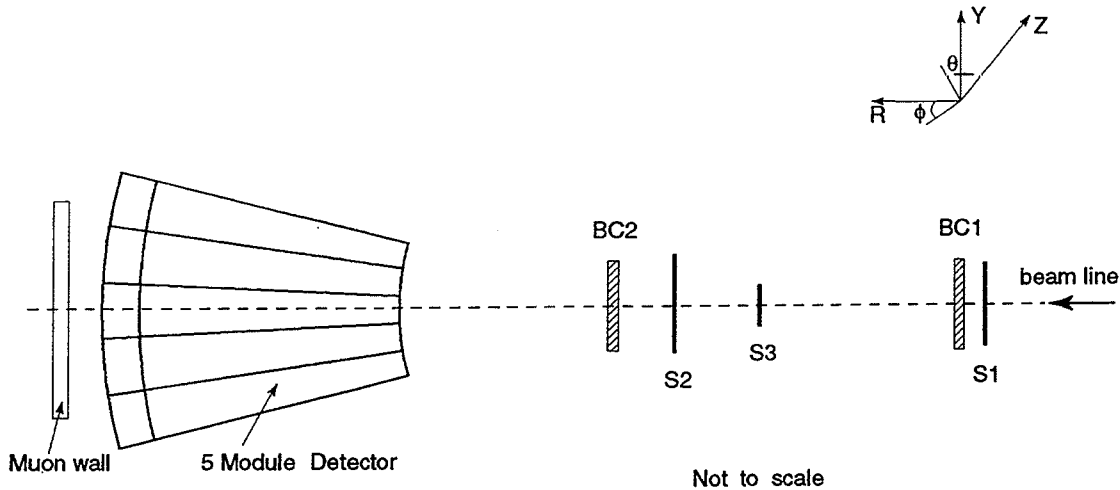| run	# events	Beam type	θ [deg]	z [cm]
33484	15205	300 GeV π^-	+10	−6
33485	15143	300 GeV π^-	+10	−8
33486	15172	300 GeV π^-	+20	−18
33487	15150	300 GeV π^-	+20	−20
33489	≈15000	300 GeV π^-	+30	−36

Table 1: Runs and orientations of the calorimeter.

The standard read-out, using charge integrating ADCs, provides a single number for the estimation of the energy per read-out channel. To calibrate these electronics it is sufficient to measure for each channel the pedestal and a calibration curve, by injecting a set of pulses of known charge.

The FERMI read-out is different in two respects: the signal is sampled every 25 ns, providing information on the pulse amplitude as a sequence of numbers, and the measurements are not linear due to the signal compression. In the present system, the phase of the trigger is not synchronized with the ADC clock, so that the time jitter is uniformly distributed in a clock period. In future applications at collider experiments, the clock will be phase locked with the beam crossing time so that the jitter will be much reduced.

The analysis thus requires two steps. The first step is to construct a lookup table for each channel to linearize the measurements. The construction of lookup tables requires in turn a detailed pulse shape reconstruction. This is described in the remainder of this section. The second step is to combine the samples of one channel to obtain an estimate of the energy released in each channel. This is discussed in the next section.
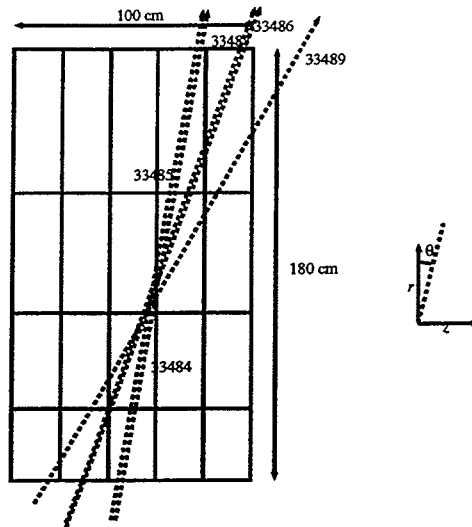
Figure 7: Impact points and direction of the beam in the five runs considered in this analysis.

The calibration was performed using charge injection pulses. During the data taking period there was one dedicated run taken with PPG charge injection with 14 different pulse amplitudes, herein labeled as PPG2–PPG15. Few cuts were applied to the raw data to remove events with a pulse peak outside sample 17 through 24 and with amplitudes far from the mean or too small (< 5 ADC counts). Approximately 600 events per PPG amplitude were recorded for channels 81 through 116, 500–550 of which survived the cuts.

4.1   Pulse Shape Reconstruction

Provided that the shaper is sufficiently linear, and that neither the shaper nor the compressor exhibits time slewing effects, the shape of the pulse is independent of the amplitude.

By "shape" we denote the functional form of the pulse, modulo scaling in amplitude and translation in time. The scaling corresponds to different released charge, and the translation to different time of flights (depending on different orientations of the calorimeter). These two quantities can be estimated for each event and in the following we concentrate on the measurement of the scaling factor, that can be unambiguously converted to energy.

In this analysis the stored samples per event (time frames) are assembled to obtain the average pulse shape following an algorithm first used in [14].

Fig. 8 shows the average frames for each amplitude for a given channel, before and after decompression with a preliminary lookup table measured in the laboratory. Pedestals are calculated from a few (8-10) samples preceding the pulse and
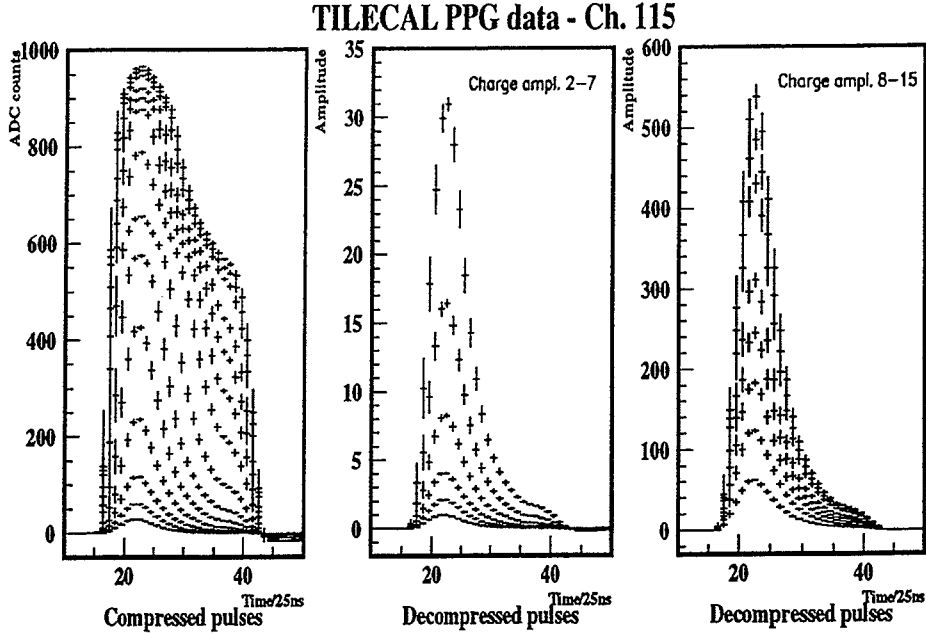
Figure 8: Average frames for compressed (left) and decompressed (middle and right) PPG pulses.

subtracted from the compressed measurements. The sampling of the pulse shape in Fig. 8 is rather coarse compared to the width of the pulse and the distributions of the sample amplitudes are widened because of the random phase of the FERMI internal clock with respect to the trigger. A much finer sampling of the shape can be obtained using a phase estimator and rebinning the samples accordingly.

The phase estimator is constructed by computing the slope between two samples straddling the peak. We take our phase estimator as $S = (s(l) - s(r))/s(p)$ where $s(l)$, $s(r)$ and $s(p)$ are the amplitudes at the samples $l = 19$, $r = 23$ and $p = 21$ respectively. The value of $p = 21$ as the peak sample is dictated by the delay fixed by the hardware. The resolution of this estimator of the phase is limited by the quantization of the ADC (times the derivative of the pulse at each point along the curve), statistics and noise. We have, somewhat arbitrarily, chosen to subdivide the bins into subbins of 1 ns.

Fig. 9 shows the amplitude-phase correlation in a 25 ns interval around the peak for two PPG levels, for compressed and decompressed data. Such correlations are used to construct Fig. 10, where we see the same data as in Fig. 8 reconstructed with a binning of 1 ns for all amplitudes. We note that all curves cross the zero line at the same point. In the lower two plots the pulses have been normalized to the
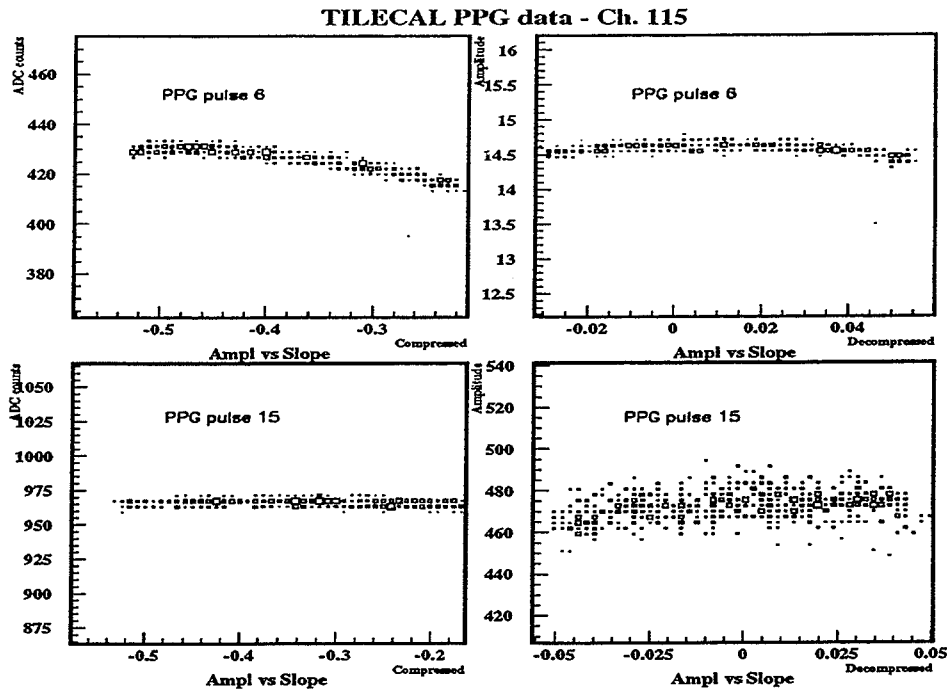
8

TILECAL PPG data - Ch. 115

Figure 9: Peak amplitude versus slope (phase estimator) for compressed (left, in ADC counts) and decompressed (right, in pC) PPG pulses PPG6 (top) and PPG15 (bottom).

same peak value to illustrate the similaritites of the shapes after decompression. More information on this approach can be found in [14].

4.2 Methods for Deriving the Lookup Tables

The lookup table should provide an inverse of the compression function so as to restore linearity with quantization errors small compared to the resolution of the calorimeter.

The most straightforward approach is to perform quasi-static measurements in the laboratory using a step function at the input and recording the step amplitude at the output. If the input can be controlled with sufficient granularity, the full lookup table can be reconstructed.

An implicit assumption underlying this approach is that the value of the compressor output at a given time depends only on the value of the compressor input at the same time. That is in general not true because of the bandwidth limitation of the compressor and, more important, of its slew rate limitation. This implies that the compressor has a non-trivial and non-linear transfer function and that
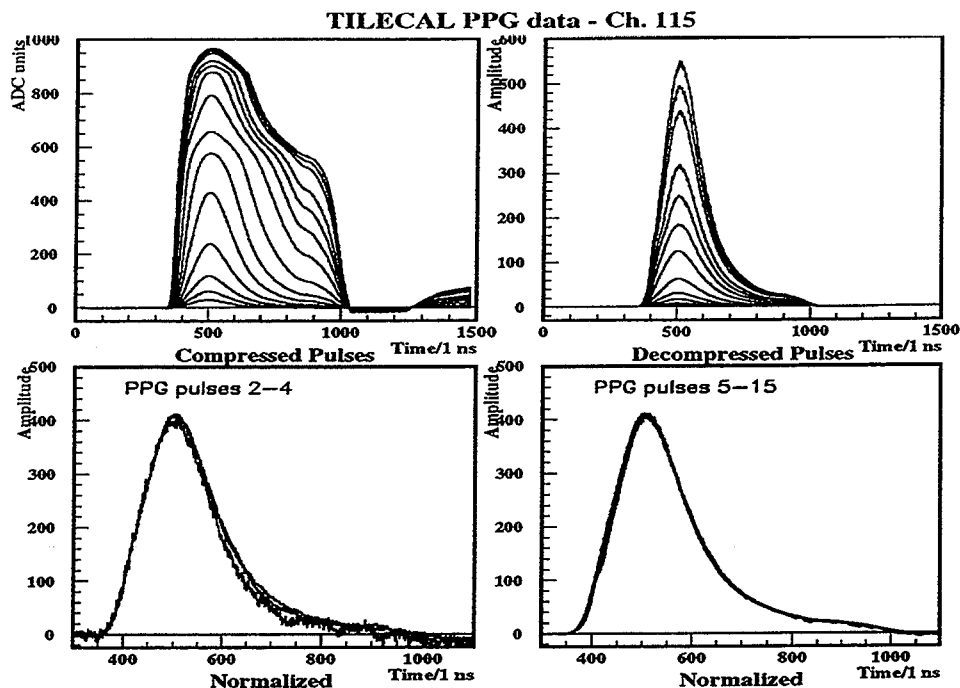
TILECAL PPG data - Ch. 115

Figure 10: Reconstructed pulse shapes. Compressed (top left) and decompressed (top right). The decompressed pulses are normalized to their peak values (bottom). Due to noise, the peak value is not sharply defined for low amplitudes, thus the discrepancy between the curves in the lower left plot.

a quasi-static measurement may not be adequate, since the compression function could depend on the input pulse shape. Another approach is therefore to pulse in situ the electronics chain with a charge injection system that closely mimics the pulses from actual data.

If we could choose the amplitudes of the charge injection system with adequate granularity and control the phase of the injected pulse with respect to the ADC clock with arbitrary precision, the amplitude and shape dependence of the compression function could be studied with great precision.

In the present set-up there were however only 14 different amplitude settings and the timing between the pulse and the ADC clock could not be fixed or measured directly, but only estimated with help of the phase estimator defined in 4.1. We had thus to use more advanced methods, using the entire pulse, to extract the required information from the calibration data.
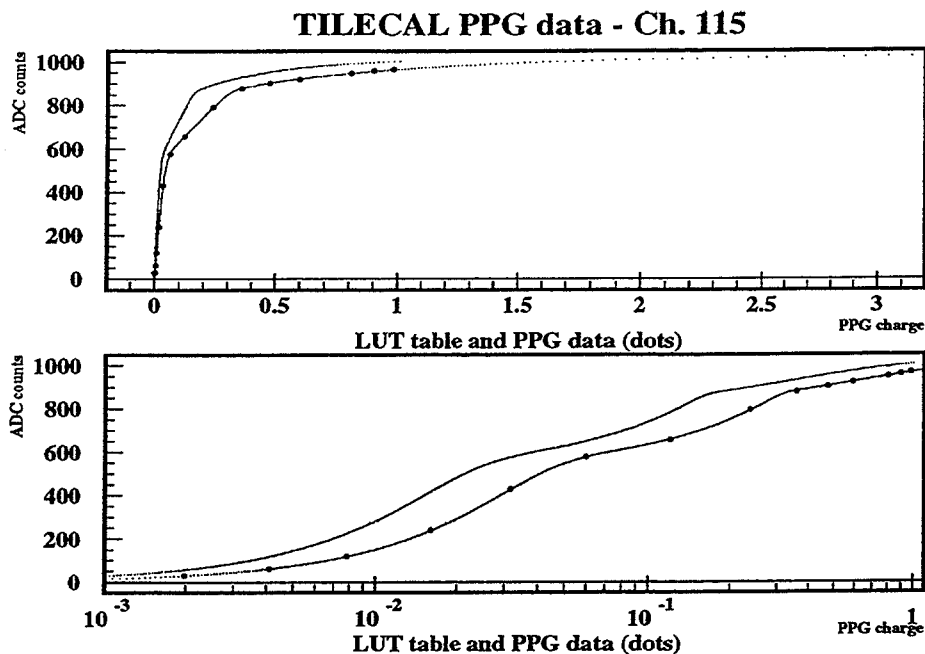
TILECAL PPG data - Ch. 115

Figure 11: Model LUT (higher curve) compared to stretched LUT (lower curve) from three parameter fit in linear (top) and logarithmic scale (below). PPG pulses are shown as fat dots.

4.2.1 A Three Parameter Fit

The different gains of each individual compressor could vary slightly due to spread in component values, mostly in the supporting circuits. The values of the cutoff voltages could also vary. To the first order these effects can be taken into account by taking a model lookup table V_{model} measured in the laboratory quasi-statically as mentioned above and distorting it slightly, by stretching and translating.

In this method we use only the peak amplitude values and the nominal charge of the PPG pulses. A parabolic fit is made to the peak region of the pulse shape to find an estimate of the peak value at zero phase. The extrapolation of the PPG peak amplitudes towards zero intercepts the charge axis at a non-zero value, q_0, which is the first parameter. The model lookup table, converting ADC-values into charge, is then linearly stretched in the charge and ADC variables, defining two more parameters, α and β, respectively. The distance between the stretched lookup table $V(k) = \alpha V_{model}(\beta k) + q_0$ and the PPG points is minimized with respect to these three parameters

$$\min_{\alpha,\beta,q_0} \chi^2 = \sum_n \left(\alpha V_{\text{model}}(\beta k_{\text{PPGn}}) - (q_{\text{PPGn}} - q_0) \right)^2.$$

The result is displayed in Fig. 11 where the unstretched and stretched model lookup table are plotted together with the measured PPG mean pulse peaks. The PPG data do not span the dynamic range of the compressors as well as the test beam, thus the lookup table is linearly extrapolated up to the highest values. This introduces an additional uncertainty for the channels measuring the highest energy in the test beam.

4.2.2 Pulse Shape Comparison

A more sophisticated method uses the fact that in a perfectly linear system the shapes of the pulses are identical, modulo a scaling factor. In case of the PPG data the scaling factor is known as the charge injected; it is labelled E_n.

In the procedure outlined below we assume a knowledge a priori of the lookup table $V(k)$ for a limited range of ADC counts. For this we use laboratory measurements of a typical channel. This choice is not critical, since for low values of the ADC counts the lookup table is linear.

Denote the pulse shapes, reconstructed as described in section 4.1, $s_n(i)$, where i indexes the time in bins of 1 ns, and n enumerates the different PPG amplitudes. We need to choose one such pulse as our reference, small enough to reside entirely within the first slope of the lookup table but large enough to stand clear of noise; this pulse is referred to as $s_{\text{ref}}(i)$.

Divide the ADC-axis into intervals between successive peak values of s_n, $k_{\text{max},n} = \lfloor \max_i s_n(i)$, where $\lfloor s_n(i)$ represents the ADC quantized value corresponding to $s_n(i)$. For each such interval $(k_{\text{max},n-1}, k_{\text{max},n}]$ we use s_n and s_{ref} to determine the updated lookup table.

The reference pulse $s_{\text{ref}}(i)$ is scaled up to the scale of the pulse under consideration. Because of shape invariance, this should correspond to the compressor input when it produces the compressed pulse s_n on the output:

$$V(\lfloor s_n(i)) = \frac{E_n}{E_{\text{ref}}} V(\lfloor s_{\text{ref}}(i)),$$

where V denotes the true (ideal) lookup table, and E_{ref} the (injected) charge of the reference pulse.

To build the modified lookup table, $V_{\text{new}}(k)$, we need to average over all time steps (i) such that $\lfloor s_n(i) = k$. We require at least one value from the leading edge and one from the trailing edge to contribute to the determination of each ADC value. Since $s_n(i)$ is discrete in i, it might skip ADC-values on either edge of the pulse. Therefore we define the extension of $s_n(i)$ into the continuous domain by interpolation, $s_n(t)$. Finally we get:

$$V_{\text{new}}(k) = \frac{1}{2}\frac{E_n}{E_{\text{ref}}}\left(V\left(\mathsf{s}_{\text{ref}}\left(t_{\text{leading}}\right)\right) + V\left(\mathsf{s}_{\text{ref}}\left(t_{\text{trailing}}\right)\right)\right).$$

Because of slew rate problems present in the compressor used in the 1995 test beam run, the invariance of the pulse shape for different amplitudes is only approximate. Parts of the pulse rising or falling at different rates are compressed slightly differently. The effect is to give separate compression functions for the rising and falling edges of the pulse and to add amplitude dependent distorsions.

The lookup table built above is the one minimizing the pulse shape dependence on the amplitude, according to the least square minimization method.

The residual dependence of the pulse shape on the amplitude might give a non-linearity for any given amplitude estimator which may take different forms for different estimators. The approach taken here is to compute the value of a given estimator for each PPG step using the V_{new} above. The values so calculated (F_n) are used to iteratively refine the correction factors for the lookup table (applicable for the given amplitude estimator):

$$V_{\text{lin}}(k) = V_{\text{new}}(k)L_n \qquad k \in (k_{\text{max,n-1}}, k_{\text{max,n}}],$$

where

$$L_n = \frac{F_{\text{ref}}}{E_{\text{ref}}}\frac{E_n}{F_n}.$$

As a result of this operation, discontinuities may appear in the lookup tables at the interface point between the ADC values linearized with two different pulse levels, as the factors L_n and L_{n-1} are in general not equal. In order to correct for this effect, a factor α_n is defined as:

$$\alpha_n = \frac{V_{\text{lin}}(k_{\text{max,n}}) - V_{\text{lin}}(k_{\text{max,n-1}})}{V_{\text{new}}(k_{\text{max,n}}) - V_{\text{new}}(k_{\text{max,n-1}})}$$

and V_{lin} is recalculated iteratively as:

$$V_{\text{lin}}(k) = V_{\text{lin}}(k-1) + \alpha_n(V_{\text{new}}(k) - V_{\text{new}}(k-1)).$$

When the full V_{lin} has been recomputed, new values for the F_n are obtained.

Using the new F_n, the above procedure is repeated, always starting from the original V_{new}. After three iterations, the V_{lin} obtained is taken as final result.

5. Energy Estimation

The energy content (or pulse amplitude) of each single cell is estimated from a subset of the sixty samples of a FERMI time frame; this procedure is called filtering. The optimum filtering algorithms both with linear and non-linear filters have been studied in detail in [15, 16, 17, 18, 19, 20]. Linear FIR (Finite Impulse
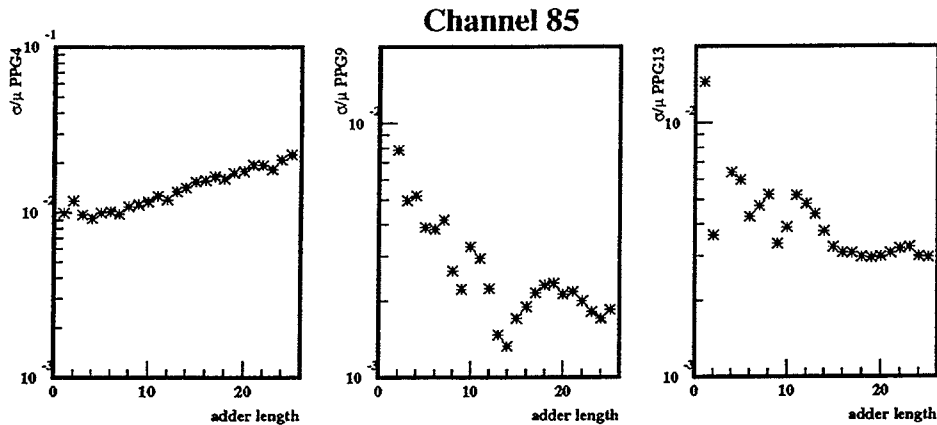
Figure 12: Resolution vs. adder length for three different PPG amplitudes, using pulse shape comparison lookup tables.

Response) filters consist of a finite number of coefficients multiplying the samples. Here we consider only adders, filters with unit coefficients.

From a general point of view, there are four dominant sources of degradations in the energy measurements of a sampled system: the electronic noise, the quantization error, the time jitter of the event and the pile-up coming from other events. In the condition of a test beam, the last term can be made negligible, controlling the beam intensity and removing overlapped events. For pulser events, this source does not exist at all.

The measurement of energy in presence of different sources of noise may lead to conflicting requirements on the filters. Generally speaking, long filters are requires to suppress the contribution from jitter, while shorter filters may be more appropriate to suppress the electronic noise. The quantization error in presence of a non-linear quantization function follows a complex pattern strongly dependent on the details of the pulse and of the filter.

A simple, but quite effective, approach is the use of adders, varying the filter length. An adder suppresses the time jitter influence if it is long enough to include both the leading and the trailing edge of the pulse. Furthermore, it has an averaging effect on noise, that, under appropriate conditions, may lead to its reduction.

Therefore, for each event, the pedestal is calculated from the average of the first few (8-10) samples. After pedestal subtraction, each sample is decompressed using its lookup table. The adder is slid along the decompressed pulse until it reaches the maximum. Adders of length 1 through 25 have been considered.
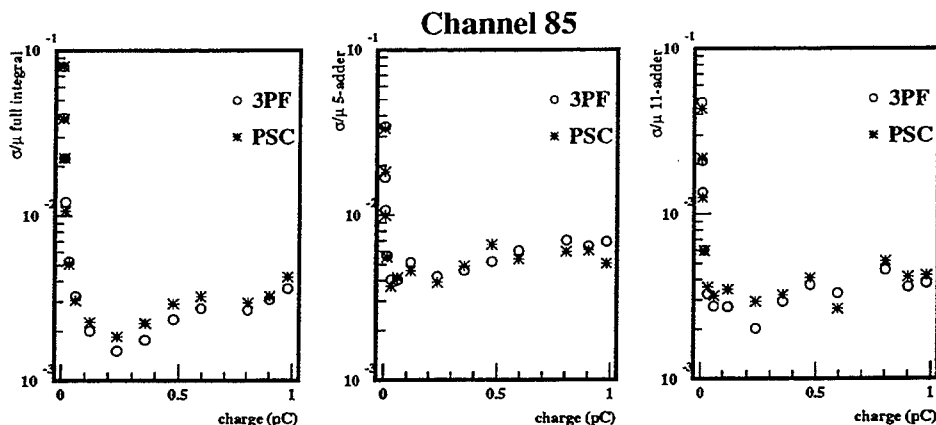
14

Figure 13: Resolution vs. PPG amplitude for full integrator and adders of lengths 5 and 11.

6. Measurement of Resolution

6.1 Single Channel Resolution

The intrinsic resolution of the two calibration methods is measured through the resolution of the charge injection data, using the energy estimates described above. We also look at the deviations from linearity of reconstructed data.

In Fig. 12 the resolution is plotted versus adder length for three different amplitudes, using pulse shape comparison lookup tables. The dependence of the resolution on the adder length is different for different amplitudes, due to different combination of the above mentioned error sources. For low amplitudes, the dominant source of uncertainty is noise, that grows with the adder length. For larger pulses noise is less significant, hence time jitter and quantization errors are predominant.

In Fig. 13 the resolution is plotted versus amplitude for full integrals (adder length 25) and adder lengths of 5 and 11. Except for the smallest amplitudes, the intrinsic resolution is always below 0.44 %. It is difficult to discern any difference between the three parameter fit method (o) and the pulse shape comparison method (*).

In Fig. 14 the resolution of all channels is histogrammed, for the case of an adder of length 11, using the two different lookup tables. The distributions are not significantly different.

In Fig. 15 the deviation from linearity vs. amplitude for a few channels is plotted for the two methods. In Fig. 16 the deviations from linearity for all channels are
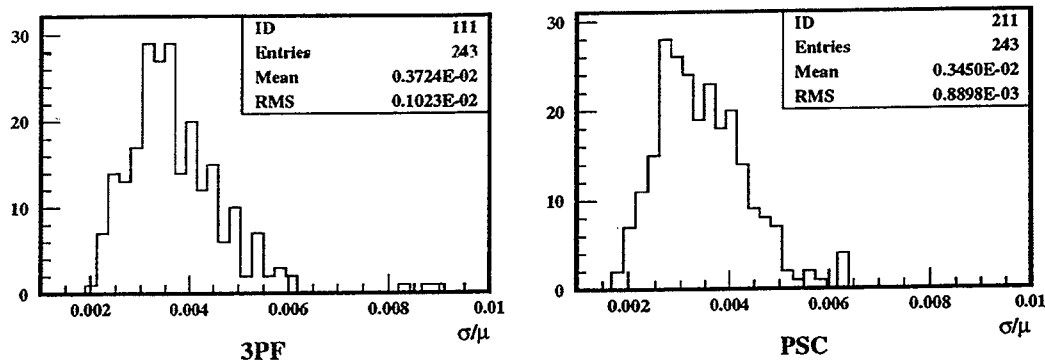
Figure 14: Resolution for all channels with adders of length 11 using three parameter fit (left) or pulse shape comparison (right). PPG pulses below an amplitude of 0.07 pC have been cut.

histogrammed for both methods. The pulse shape comparison clearly gives a better linearization than the three parameter fit.

6.2 Event Sample Selection

For the analysis those π^- runs at 300 GeV which involved as many FERMI-equipped channels as possible and which have the smallest possible intrinsic fluctuations in order to make the comparison of the read-outs as sensitive as possible were used.

In order to remove the electron and muon contaminations from the beam we demand that between 60% and 95% of the energy be deposited in the first two sampling depths of the calorimeter and that the total energy be above a threshold.

6.3 Resolution with Fermi and the Standard Electronics

The most straightforward method of comparing the two read-out systems would use the energy resolutions obtained using the channels that were equipped with both types of electronics. Due to the large leakage into channels without FERMI (mostly into the neighbouring modules) the fluctuations of the deposited energy is quite large.

To account for the leakage we reconstruct the energy released in the 173 channels with standard read-out only, in addition to the 27 equipped with FERMI. In all runs the fraction of the total energy deposited in the FERMI equipped channels varies between 75 and 90%.

The resolution in both cases can be written as a quadratic sum of one energy dependent term and three or four constant terms. The energy dependent term is
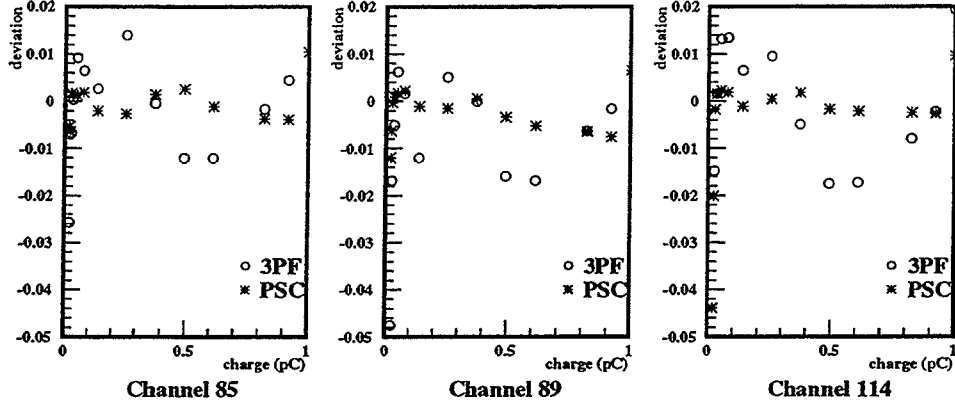
Figure 15: Deviation from linearity vs. amplitude for three different channels.

the intrinsic spread in the measurements, depending only on the calorimeter, and the constant terms are contributions from leakage, from the electronics calibration errors, and, when considering the sum of standard and FERMI channels, from interchannel calibration errors. Noise contribution is not relevant at the energies considered and therefore is not included:

$$R_S = \left.\frac{\sigma}{E}\right|_S = \frac{a}{\sqrt{E}} \oplus C_{\text{leakage}} \oplus C_{S173} \oplus C_{S27},$$

$$R_F = \left.\frac{\sigma}{E}\right|_F = \frac{a}{\sqrt{E}} \oplus C_{\text{leakage}} \oplus C_{S173} \oplus C_{F27} \oplus C_{\text{misintercalib.}},$$

where the subscript S denotes standard read-out and F denotes FERMI.

When comparing only 27 channels, the C_{S173} term does not contribute while lateral leakage in the ϕ direction makes C_{leakage} large; this term is however in common between the two different read-out electronics. When summing 200 channels the C_{S173} term gives a sizeable contribution while C_{leakage} is comparably smaller.

The quality of the electronics and our calibration methods is measured with the signed quadratic difference, $\delta = \pm\sqrt{\left|\left(\left.\frac{\sigma}{E}\right|_F\right)^2 - \left(\left.\frac{\sigma}{E}\right|_S\right)^2\right|}$, between the resolutions, where negative sign of δ indicates that the standard term under the square root is larger than the FERMI term. This gives an estimate of the FERMI electronics contribution to the resolution. In order to assign an error to δ, the high correlation between the measurements with FERMI and the standard electronics has to be taken into account.
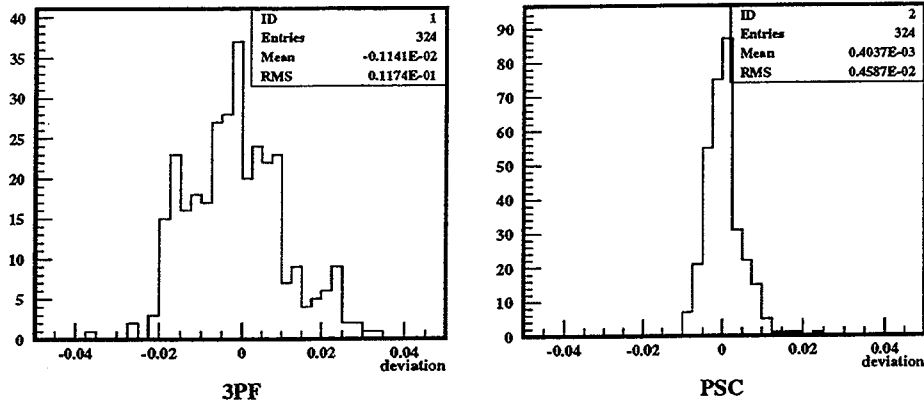
17

Figure 16: Deviations from linearity for all channels. PPG pulses with an amplitude below 0.025 pC are removed.

6.4 Measured Resolutions

In Table 2 and Table 3 we see that the three parameter fit method ("stretching") is slightly worse compared with the standard read-out. Most likely that is due to the limitation of linearity in the lookup table shown in Fig. 16. On the other hand, the method based on linearized pulse shape comparison performs significantly better than the standard electronics, at least for an adequate filter length. This is demonstrated in Table 3. The main reason is likely to be the higher control on linearity guaranteed by this method.

With some approximation, the performance of FERMI can be summarized in a quadratic reduction of 1% of the constant term in the resolution.

7. Summary

A module of the prototype of the ATLAS hadronic calorimeter has been succesfully tested with a preliminary version of the FERMI read-out system including a compressor and a sampling ADC.

The charge injection system has been used to calculate separately for each channel lookup tables that minimize amplitude dependent distortions and non-linearity. These techniques in conjunction with the use of linear adders to process the sampled data, reduce the constant term in the energy resolution as compared to the one obtained with standard integrating ADCs.

18

run	33484	33485	33486	33487	33489
stand.	5.16 ± 0.06	5.73 ± 0.08	4.36 ± 0.05	4.36 ± 0.05	4.67 ± 0.06
3PF 5	5.55 ± 0.07	6.13 ± 0.09	4.84 ± 0.06	4.75 ± 0.06	4.73 ± 0.06
3PF 11	5.39 ± 0.07	5.96 ± 0.09	4.61 ± 0.05	4.58 ± 0.05	4.69 ± 0.05
3PF I	5.35 ± 0.07	5.87 ± 0.08	4.51 ± 0.05	4.49 ± 0.05	4.57 ± 0.05
PSC 5	5.14 ± 0.06	5.81 ± 0.08	4.41 ± 0.05	4.42 ± 0.05	4.71 ± 0.05
PSC 11	5.04 ± 0.06	5.59 ± 0.07	4.31 ± 0.05	4.32 ± 0.05	4.61 ± 0.05
PSC I	5.03 ± 0.06	5.60 ± 0.07	4.20 ± 0.05	4.25 ± 0.05	4.48 ± 0.05

Table 2: Resolutions (in %) for standard electronics (stand.), and FERMI with the look-up tables reconstructed with the three parameter fit (3PF) and the pulse shape comparison (PSC) methods for 5-adder, 11-adder and full integrator (I) for five runs (cf. Fig. 7), using 200 channels.

run	33484	33485	33486	33487	33489
3PF 5	2.03 ± 0.06	2.19 ± 0.07	2.10 ± 0.05	1.89 ± 0.06	0.77 ± 0.07
3PF 11	1.56 ± 0.05	1.67 ± 0.07	1.48 ± 0.05	1.42 ± 0.07	0.48 ± 0.10
3PF I	1.42 ± 0.06	1.28 ± 0.11	1.17 ± 0.07	1.10 ± 0.10	-0.95 ± 0.08
PSC 5	-0.44 ± 0.15	0.98 ± 0.10	0.63 ± 0.10	0.71 ± 0.14	0.65 ± 0.07
PSC 11	-1.10 ± 0.05	-1.22 ± 0.07	-0.68 ± 0.08	-0.56 ± 0.17	-0.73 ± 0.06
PSC I	-1.17 ± 0.04	-1.21 ± 0.09	-1.18 ± 0.07	-0.98 ± 0.11	-1.32 ± 0.05

Table 3: Quality measure of the read-out, δ, expressed as the signed quadratic difference with the standard resolution, for the look-up tables reconstructed with the three parameter fit (3PF) and the pulse shape comparison (PSC) methods for 5-adder, 11-adder and full integrator (I) for five runs (cf. Fig. 7), using 200 channels.

References

[1] M. Bosman et al., Developments for a scintillator tile sampling hadron calorimeter with "longitudinal" tile configuration, CERN/DRDC/93-3, 1993.

[2] F. Ariztizabal et al., Nucl. Instr. and Meth. **A349**, 384 (1994).

[3] E. Berger et al., Construction and performance of an iron-scintillator hadron calorimeter with longitudinal tile configuration, CERN/LHCC/95-44, 1994.

[4] E. Berger et al., A measurement of the energy loss spectrum of 100 GeV muons in iron, CERN/PPE/96-115, 1996, Accepted for publication in Z. Phys.

[5] Z. Ajaltouni et al., Response of the ATLAS tile calorimeter prototype to muons, CERN/PPE/173-96, 1996, Accepted for publication in Nucl. Instr. and Meth. A.

[6] ATLAS Tile Collaboration, The ATLAS tile calorimeter technical design report, CERN/LHCC/96-42, ATLAS TDR 3.

[7] H. Alexanian et al., Nucl. Instr. and Meth. **A357**, 306 (1995).

[8] R. Benetta et al., Status report on the FERMI project, CERN/LHCC/95-28.

[9] C. Svensson and J. Yuan, IEEE Journal on Solid State Circuits and Systems **29**, 866 (1994).

[10] P. W. Cattaneo and G. Polesello, Results of the common testbeam RD16-RD34, FERMI Note # 36.

[11] P. W. Cattaneo, Results of the common testbeam RD16-Accordion calorimeter, FERMI Note # 40.

[12] FERMI Coll., Results of the testbeam of RD16 (FERMI) with electromagnetic and hadronic calorimeter prototypes, FERMI Note # 42, ATLAS Note/DAQ # 42, CMS/TN Note # 95-009.

[13] A. Beer et al., Nucl. Instr. and Meth. **A224** (1984).

[14] P. W. Cattaneo, A technique of signal shape reconstruction in sampled system, FERMI Note # 45, Submitted to Signal Processing.

[15] P. W. Cattaneo, Nucl. Instr. and Meth. **A373**, 93 (1996).

[16] S. J. Inkinen, FIROSMIN 3.1 users guide, FERMI Note # 24.

[17] S. J. Inkinen et al., Nonlinear filters for pulse amplitude extraction in FERMI, in *Proc.IEEE Nuclear Science Symposium*, pages 687–691, 1994.

[18] S. J. Inkinen and J. Niittylahti, IEEE Transactions on Circuit and Systems-II: Analog and Digital Signal Processing **42**, 663 (1995).

[19] H. Alexanian et al., Nucl. Instr. and Meth. **A357**, 318 (1995).

[20] N. Launay, C. de la Taille, and L. Fayard, Noise improvement with multiple samples, ATLAS Note/CALO # 24.